Electrolyte Effects on the Stability of Ni-Mo Electrocatalysts Employed for Water Splitting

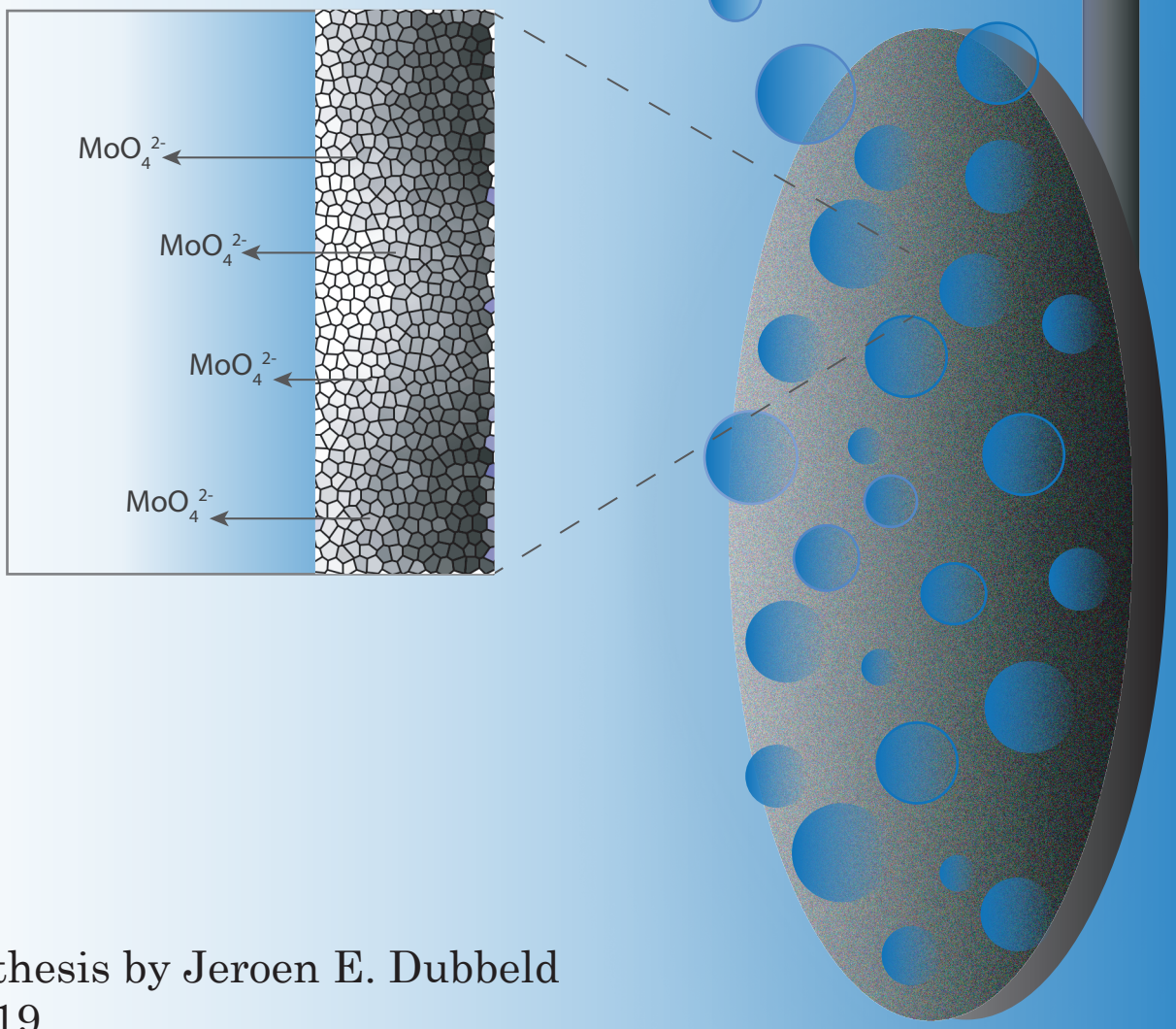

Master thesis by Jeroen E. Dubbeld
2018/2019

Electrolyte Effects on the Stability of Ni-Mo Electrocatalysts Employed for Water Splitting

Master thesis

Jeroen E. Dubbeld

6028454

Daily Supervisor: J.H.J Wijten

First Examiner: Bert M. Weckhuysen

Second Examiner: Florian Meirer

Inorganic Chemistry and Catalysis

Faculty of Science

Debye Institute for Nanomaterials Science

Utrecht University

2018/2019

Abstract

The Ni-Mo electrocatalyst has been recognised as one of the most promising earth-abundant materials for the alkaline hydrogen evolution reaction. In recent research it was found that during electrolysis of water, molybdenum migrates to the surface of the cathode and leaches out into the electrolyte solution as molybdate. Furthermore, the cation used in the electrolyte influenced the strength of the leaching.
In this thesis, the influence of different cations and the hydroxide concentration on the leaching of molybdenum was researched in depth. By varying the pH between 8 and 14.8 and using lithium, sodium and potassium as cation, the effects on Ni-Mo surface change were studied systematically. The Ni-Mo electrocatalysts were synthesized using electrodeposition and were employed for 3-day electro-catalysis at a current density of -10 mA/cm^2. The surface displayed changes in roughness and composition, when studied before and after catalysis. This surface change was mainly studied with SEM-EDX, capacitance measurements, ICP-AES and liquid AFM. Transient chrono-potentiometry, linear sweep voltammetry and GC were used to study the efficiency changes when influenced by a change in electrolyte solution.

The hydroxide concentration is the main incentive that pushes the molybdenum equilibrium towards molybdate, overcoming the reductive potential around the electrode. It was noticed with EDX and capacitance measurements that when using potassium as cation the amount of molybdenum that leached from the electrode doubled, most likely due to a solubility effect.
The activation time observed for the catalyst is caused by the increase in surface area due to leaching of molybdenum as was seen with liquid AFM. Further proof was obtained when the faradaic efficiency was calculated, where an efficiency of up to 115% was obtained. This efficiency over 100% was explained to be due to extra hydrogen production from the molybdenum oxidation.
The high surface area due to the leaching of molybdenum appears to be the most important facet for its low overpotentials. Molybdenum is necessary in certain amounts to circumvent the formation of nickel hydrides.
Increasing the current density to -500 mA/cm^2 showed far lower molybdenum loss in 1M KOH. SEM displayed a restorative effect on the Ni-Mo alloy, restoring cracks that were there before catalysis.

"And what will they burn instead of coal?"

"Water," replied Harding.

"Water!" cried Pencroft, "water as fuel for steamers and engines! Water to heat water!"

"Yes, but water decomposed into its primitive elements," replied Cyrus Harding, "and decomposed doubtless, by electricity, which will then have become a powerful and manageable force, for all great discoveries, by some inexplicable laws, appear to agree and become complete at the same time. Yes, my friends, I believe that water will one day be employed as fuel, that hydrogen and oxygen which constitute it, used singly or together, will furnish an inexhaustible source of heat and light, of an intensity of which coal is not capable. Someday the coal-rooms of steamers and the tenders of locomotives will, instead of coal, be stored with these two condensed gases, which will burn in the furnaces with enormous calorific power. There is, therefore, nothing to fear. As long as the earth is inhabited it will supply the wants of its inhabitants, and there will be no want of either light or heat as long as the productions of the vegetable, mineral or animal kingdoms do not fail us. I believe, then, that when the deposits of coal are exhausted we shall heat and warm ourselves with water. Water will be the coal of the future."

"I should like to see that," observed the sailor.

"You were born too soon, Pencroft,"

Jules Verne - The Mysterious Island (1874)

Table of Content

1. **Introduction** 1

1.1 Energy storage: Hydrogen 2

1.1.1 Hydrogen as fuel 2

1.2 Electrochemistry 3

1.2.1 Electrolysis of water 6

1.2.2 Electrocatalysts 6

1.3 Nickel-molybdenum HER catalyst 8

2. **Methodology** 10

2.1 Synthesis 17

2.1.1 Electrodeposition 17

2.2 Electro-catalysis 18

2.3 Electrochemical analysis techniques 20

2.3.1 Transient chrono-potentiometry 14

2.3.2 Cyclic Voltammetry 15

2.3.3 Linear Sweep Voltammetry 16

2.4 Characterisation and measurements 17

2.4.1 Scanning electron microscopy - Energy Dispersive X-ray spectroscopy 17

2.4.2 Inductive Coupled Plasma Atomic Emission Spectroscopy 17

2.4.3 Atomic Force Microscopy 18

2.4.4 Faradaic efficiency – Gas chromatography 18

3. **Results** 19

3.1 The Ni-Mo catalytic activity 19

3.2 Ni-Mo stability 21

3.2.1 Structural changes catalyst surface 22

3.2.2 Electrolyte solution changes 27

3.2.3 Current effects 29

3.2.4 Molybdate spiked electrolyte 33
3.3 *In-situ* analysis 35
3.3.1 *In-situ* liquid AFM analysis 35
3.4 Ni-Mo electrolytic selectivity 38
3.4.1 Faradaic efficiency 38
3.4.2 Linear Sweep Voltammetry 39
4. **Summary** 48
5. **Conclusions** 50
6. **Outlook** 44
7. **Acknowledgements** 45
References 46
Appendices 57
Appendix A – activation times 57
Appendix B – SEM images (roughening) 59
Appendix C – ICP-AES 61
Appendix D – *in-situ* UV-vis cell 55
Appendix E – AFM images 56

1. Introduction

Society's demand for energy is ever increasing as globally more households gain availability to energy for heating and electrical devices (77,7% in 2000, 87,4% in 2016) [1]. In addition, existing households and industries worldwide require more energy to satisfy their increasing demand [2]. This increase in demand will need to be met using power sources that can still guarantee a future for coming generations. It would require energy generation independent on fossil fuels and without a net emission of environmental harmful products. As this realization grows, a shift towards renewable energy sources is gaining momentum and with that, the rise of wind and solar energy [3]. The European Union has responded to this transition by setting the goal of 20% of the total energy usage as renewable energy by the year 2020 [4].

Energy generation until recent years has been dominated by the burning of fossil fuels, since it can answer energy demands whenever it is necessary. This supply-on-demand by fossil fuels is favourable, but leaves a large strain on the environment due to the emission of carbon dioxide [5] and delving of resources [6].
Carbon dioxide is a known greenhouse gas of which the concentrations in the atmosphere have risen exponentially since the industrial revolution from 280 ppm in 1800 to 360 in 2000 [7]. Temperatures have been estimated to rise by 2 – 5 °C before 2100 [5], which could have devastating effects on ecosystems. The increase in carbon dioxide is a result of the excessive burning of fossil fuels for transport and energy generation. Furthermore, the fossil fuels are becoming scarcer and should be put to better use than the generation of energy, such as speciality chemical industry (medicine, paints and construction materials). To lose the dependency on fossil fuels for energy and make 'the energy transition' [8], there are some major challenges to overcome.

Renewable energy sources, such as solar and wind, are intermittent due to numerous variables that do not correspond to energy demands. Think of windy or calm weather, sunny or cloudy, day or night and an even larger contributor: summer vs. winter. Due to these irregularities, efficient and clean storage of energy has become crucial for the transition to renewables. Storage of energy would be favourable to provide energy on demand, which is now largely done with the use of fossil fuels [9]. With the growth of renewable energy production [3] this quest for the storage of energy has opened an entire new field of applications.
A wide range of methods to store renewable energy have been proposed so far [10], [11]. With examples such as the use of batteries [12], supercapacitors [13], flywheel energy storage [14], 'Pumped Hydro Energy Storage' (PHES) [15] and storage in the form of chemical bonds, such as molecular hydrogen [16]. Storage in the form of chemical bonds is a promising method that is further explored in this thesis.

1.1 Energy storage: Hydrogen

Hydrogen has the potential to become the main renewable fuel of the future. Ever since hydrogen was discovered by Henry Cavendish, people have envisioned the "Hydrogen economy"[17], [18], where hydrogen would replace all fossil fuels. Jules Verne in 'The Mysterious Island' was one of the more famous early visionaries for hydrogen [19] in 1874.
Hydrogen owes its incredible potential to one of its production methods, namely through the electrolysis of the inexhaustible resource: water. By applying a potential difference on two electrodes submerged in water, a potential can be reached which initiates the splitting of water into its elementary components. Water (H_2O) can then be converted into hydrogen (H_2) and oxygen gas (O_2) on the surfaces of electrodes [20]. These two gasses then become the carrier for the energy that has been applied on the water. As oxygen already is an abundant resource (air), the real value of the method is the production of the hydrogen gas.
Hydrogen production sites could be constructed near solar farms, hydropower facilities and wind farms to store electricity locally. When energy production is high or demand low, part of the generated electricity can be converted to hydrogen. This hydrogen, produced by electrolysis of water, is of the highest grade as no side products are formed. This in contrast to steam methane reforming, where a mixture with carbon monoxide or carbon dioxide is produced [21], although useful for syntheses like Fisher Tropsch, further refining would be needed obtain pure hydrogen.
Hydrogen, produced by electrolysis of water, is ready as fuel straight after production. However, the storage of hydrogen as fuel can bring several complications, as will be elaborated in the next section.

1.1.1 Hydrogen as fuel

Hydrogen can be stored under high pressure as a supercritical gas or cryogenically as a liquid, but these methods are highly energy intensive [22], as the boiling and critical point of hydrogen are low (21.2 K and 33 K respectively) [23]. Applications to store the gas in metals as hydrides [24] or metal-organic frameworks [25] are being explored but do not offer a solution on large scale to this day. Another way to store the produced hydrogen through electrolysis, is converting it to carbon-based fuels.
Hydrogenation of carbon monoxide or carbon dioxide to hydrocarbons, such as the Sabatier and Fisher-Tropsch reactions, are a hot-topic in catalysis [26], [27]. It offers a way to keep using our daily fossil fuel driven instruments, while producing the fuels 'carbon neutral'. Furthermore, it gives rise to the possibility to store energy in a more manageable liquid form at ambient temperatures. Carbon monoxide and dioxide is a waste product of many industries and hydrogenating it would offer a purpose in new cycle-of-use [28].

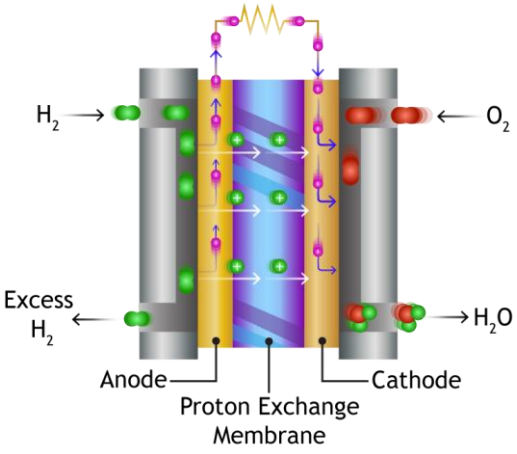

Figure 1. Proton-exchange membrane fuel cell where molecular hydrogen and oxygen are turned into electricity with water as end product [29].

For hydrogen gas to be used as a fuel it, needless to say, needs to be turned back to energy. By simply burning it, an extremely fast exothermic

reaction occurs that releases all the energy (237.2 kJ/mole), but it would not be utilisable as electricity. This is where the proton-exchange membrane (PEM) fuel cell makes its introduction (Figure *1*). This fuel cell is an electrochemical energy conversion device, that turns hydrogen and oxygen back into water and captures the energy in the form of electricity with an overall efficiency of around 60-80% [29], [30].
Water can be turned into hydrogen and oxygen by electrochemical splitting of the bonds. The study of the electrochemical behaviour of reactions such as water splitting, is categorised as electrochemistry.

1.2 Electrochemistry

Electrolysis is a subcategory of electrochemistry where energy is used to split bonds within molecules. Electrochemistry is used to study a wide range of phenomena like corrosion [31], metal/solution interfaces [32], redox reactions [33] and electrocatalysis [34]. The most famous and widely used relation in electrochemistry is that of potential, current and resistance (formula 1).

$$U(V) = I(A) \times R(\Omega) \quad (Formula\ 1)$$

Electrochemistry is often studied in an electrochemical cell, which contains two or more electrodes submersed in an electrolyte solution. An electrolyte solution defined as a conductive liquid by either dissolved salts [34], [35] or an ionic liquid itself [36]. Two types of electrochemical cells are generally recognised. The first one, the galvanic cell, produces electricity by consuming chemical energy from substances. The second is the electrolytic cell, which consumes electricity to produce chemical substances as is the case with water splitting [37].
The two electrodes, a working electrode (WE) and a counter electrode (CE), are connected to a potentiostat to facilitate and regulate the electrochemical reactions. When a desired potential is applied on the WE, charge transfer can occur between the electrode and electrolyte/analyte causing a reaction to take place. At the CE the same process occurs, only with opposite sign to balance the current (oxidative vs reductive). The potential difference between the two electrodes is variable, as a result of the applied current density.

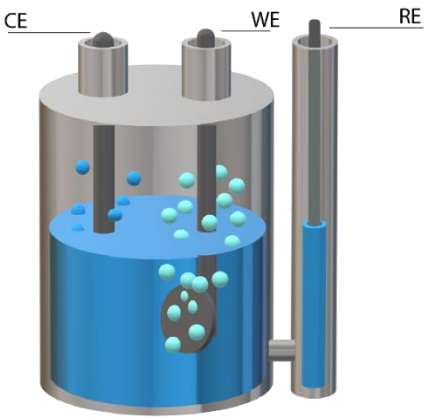

Figure 2. The three-electrode set-up

When the potential at the WE is desired to be studied, a third, reference electrode (RE) can be added (Figure 2). The RE has a known reduction potential and is connected to the WE. Nearly no current flows between RE and WE, which keeps the potential at the RE stable. Now as a current is applied between WE and CE, resulting in a potential difference at the WE, it can be studied between WE and RE. Since the RE has a stable, known potential the measured difference is only the potential at the WE [38]. The RE is often separated from the electrochemical cell by a Luggin capillary, as is shown in Figure 2. This circumvents potential changes in the liquid of the electrochemical cell to influence the RE.

The Nernst equation

A redox reaction can be initiated by overcoming its thermodynamic barrier. The energy required thermodynamically is determined by the difference in Gibbs energy (ΔG) between reactants and products. Correspondingly, the difference in Gibbs free energy is the maximum amount of energy that can be converted to mechanical work or electricity. The difference in Gibbs free energy holds a relation with potential via the Nernst equation (formula 2).

$$\Delta G = -nFE^{\circ} \quad (Formula\ 2)$$

Where ΔG is the difference in Gibbs free energy, n the number of electrons transferred in a reaction, F the Faraday constant and E° the standard potential (under standard conditions) [20]. When a potential is applied that leads to a Gibbs free energy of below zero, a reaction becomes thermodynamically favourable.
In an electrochemical cell standard conditions are rarely met due to differences in temperature, reactant concentrations and activity. Derived from Formula 2 and more extensive thermodynamic derivations the Nernst equation for non-standard conditions becomes:

$$E = E^{\circ} - \frac{RT}{nF} \ln \frac{C_{products}}{C_{reactants}} \quad (Formula\ 3)$$

Here E is to required cell potential under non-standard conditions, R the gas constant, T the temperature and C the activity of either reactants or products. The activity, C, is often simplified and replaced by the concentration of the components. This formula shows how the required potential to make a reaction thermodynamically favourable, changes under non-standard conditions. Formula 2 and Formula 3 are used to calculate when a reaction can take place. This, however, says very little about at what speed a reaction (i.e. kinetics) propagates.

Overpotential

To get the reaction to start flowing after overcoming the thermodynamic barrier (a current becomes observable), several resistances need to be overcome. These resistances are overcome by applying additional potential on the electrodes, also referred to as the overpotential (η). See Figure 3 for a schematic overview of the concept. Generally three types of overpotential are recognised which are used to overcome the resistances of the system. 1) Activation overpotential, which overcomes interfacial resistances such as the charge transfer from electrode to reactant. 2) Resistance overpotential, which deal with ohmic losses of the cell,

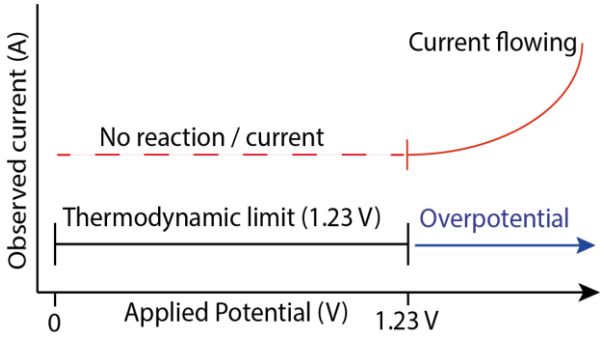

Figure 3. Schematic overview of the concept: overpotential

such as fluid resistance and heat loss. 3) Concentration overpotential, which is caused by a concentration difference between the bulk and interface. As reactants will need to be supplied constantly to the electrode surface, extra potential will need to be applied [38].All three these factors will combine in one observable overpotential on top of the thermodynamic limit, to get a current running through the system and get hydrogen production going. When large overpotentials are applied, mass transport limitations can occur. Mass transport limitations occur as electrodes become oversaturated with reactants, or reactant concentration is too low to keep up with the exchange rate of the reaction (current). Mass transport limitations generally give rise to high resistances and deviations that can be seen in current and voltage.

Capacitance

When a redox reaction occurs at an electrode surface, there is an exchange of electrons between the metal surface and the electrolyte solution. At this interphase between the metal and liquid surface a discrepancy occurs due to bulk differences. A contact plane between the liquid and metal surface forms which behaves like a transit phase from solid to liquid [39]. When a surface is or becomes charged, like an electrode, it pulls opposite charged ions to its surface and forms a single atomic immobile layer called the inner-Helmoltz layer. The immobile layer follows the direct curvature of the metal surface down to the atomic level [38]. The second, outer-Helmholtz layer becomes more mobile and also contains equally charged ions and flows over into a diffusive layer (Figure 4). These two Helmholtz layers together, are called the electric double layer [40].

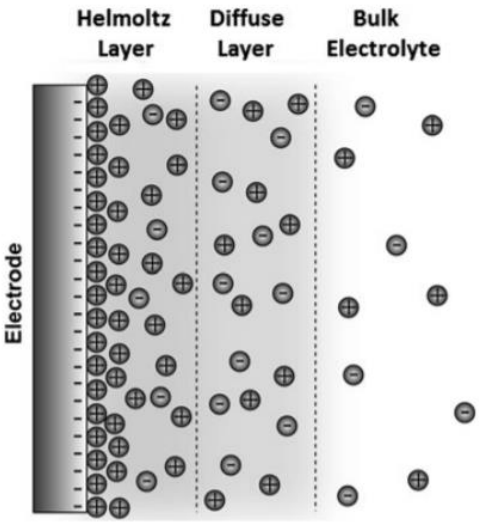

Figure 4. Schematic of the electric double layer, consisting of the two Helmholtz layers and a diffusive layer [38].

When charging an electrode, ions move and adhere to the surface in the electric double layer. In non-faradaic regions, with concentrated electrolyte solutions, the electrode its charge becomes compensated by the electrolytes. As the surface charge gets compensated, energy is stored at the interphase, which would be released when the charge on the electrode is removed [13]. This measure of charging and discharging is called the capacitance and is expressed in units of Farads ($s^4 \cdot A^2 \cdot m^{-2} \cdot kg^{-1}$). The capacitance can be described as the amount of charge that an electrode surface can hold and is measured with electrochemical analysis techniques likes cyclic voltammetry [35] and electrochemical impedance spectroscopy [41].

The capacitance is of interest as it gives a measure of the electrochemically active surface area (ECSA) of an electrode [42]. It contains information about the catalytic available sites for electrochemical reactions and also for the real surface area instead of a geometric surface area of an electrode. For a reaction like the electrolysis of water to molecular hydrogen and oxygen, the measure of capacitance can give a lot of information about both the electrode and the reaction efficiency.

1.2.1 Electrolysis of water

For a liquid to be sufficiently conductive it needs to contain both positive and negative charged species/ ions. These charged species are generally supplied by either acidifying or alkalifying the solution with either sulfuric acid or alkali-metal hydroxides. Hydroxides and protons have the highest mobility in aqueous solutions [43], which lowers fluids resistances for optimal performance.
The splitting of water can occur in both alkaline and acidic solutions with both their unique pathways. However, this thesis mainly focusses on the alkaline route as acidic solutions offer few efficient and catalytic stable metals for the anode [44], [45].

The HER is a reaction that requires a potential to overcome the thermodynamic barrier as described in the last section. The potential difference needed for the splitting to occur is calculated using half-reactions. The water-splitting reaction in alkaline media consists of two half-reactions, with one occurring at each electrode:

OER:	$4\,OH^- \rightarrow 2\,H_2O + O_2 + 4\,e^-$	E^o_{anode} = 0.401 V (vs RHE)
HER:	$4\,H_2O + 4\,e^- \rightarrow 4\,OH^- + 2\,H_2$	$E^o_{cathode}$ = - 0.828 V
Overall:	$2\,H_2O \rightarrow 2\,H_2 + O_2$	E^o_{total} = 1.229V (E^o_{anode}- $E^o_{cathode}$)

At the anode, the 'oxygen evolution reaction' (OER) takes place, forming oxygen gas. At the cathode, the hydrogen evolution reaction (HER) takes place, forming hydrogen gas [20], [46]. The anode and cathode electrode offer surface for the reaction to take place. By adsorbing water (HER) and hydroxide (OER) at the surfaces, a charge transfer between the electrode and the reactants can occur. The electrode material can catalyse the reaction to occur at lower overpotentials. By selecting a material for the electrode that specifically lowers the energy required for a reaction to propagate, it becomes an electrocatalyst.

1.2.2 Electrocatalysts

In regular catalysis a catalyst assists in lowering an activation energy for a thermodynamic more favourable product (at a given pressure/temperature). In electro-catalysis however, a potential is applied on a catalyst/electrode that can push against a thermodynamic favourable direction. The electrocatalyst assists in lowering the overpotential needed to make the thermodynamically unfavourable reaction occur. The hydrogen evolution reaction (HER) is one of these thermodynamic unfavourable reactions, where an applied potential assists in the production of molecular hydrogen.
Electro-catalysis takes place at a surface which catalyses a reaction. The surface in this case is the surface of an electrode, that can be doped or coated for better performance. The main goal of the catalyst is lowering the activation energy for charge transfer at the interface by effectively adsorbing species [47]. By lowering the activation energy, it reduces the overpotential of one or more half-reactions.

The effectiveness of a catalyst is explained by the so-called volcano plot, as seen in Figure 5 [48], [49]. In this figure the exchange current as a function of the M-H binding strength is displayed. The exchange current density is the rate of reaction at zero external potential applied, or in other words how fast the reaction occurs at standard conditions [31]. As can be seen in this figure, platinum has the highest activity for all pure metallic electrodes [50], [51]. Platinum adsorbs hydrogen strong enough for it to form H_2, but also weak enough to subsequently desorb it.

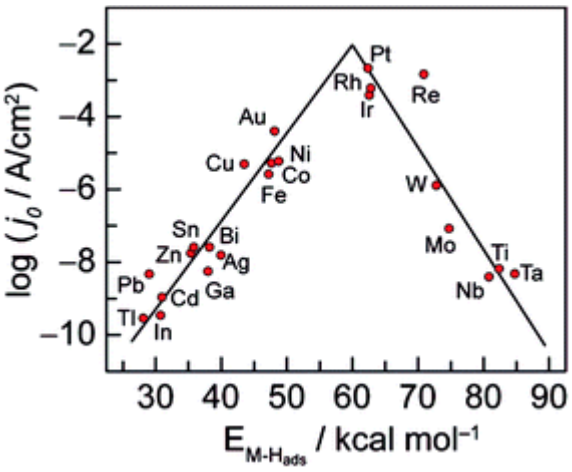

Figure 5. Volcano-plot for the HER based on the Sabatier principle. By Y. Yan et al [51].

The volcano plot is constructed at zero applied potential, which makes accuracy of some metals questionable, as in practice the HER does not occur at zero applied potential. Metals to the right of platinum (W and down) tend to be in their oxide forms at zero applied potential. The activity of those oxide metals can increase significantly at a reductive potential where they exist as metals.

The catalytic steps from adsorption of water to desorption of hydrogen have been studied extensively [45], [48]. Three steps are recognised for the adsorption and desorption at the surface of the anode. First is the Volmer step, where water adsorbs and, with an electron, splits into an adsorbed hydrogen atom and a hydroxide ion. Upon interaction with another adsorbed hydrogen atom, the hydrogen can form and release as molecular hydrogen via the Tafel mechanism. If the adsorbed hydrogen atom interacts with another water molecule and electron, it can split directly into a hydroxide ion and molecular hydrogen (Heyrovski mechanism).

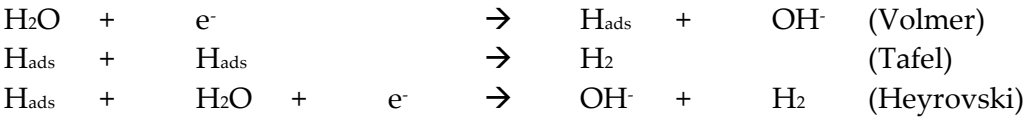

In these mechanisms, the Volmer step always needs to occur first, which makes two routes possible: the Volmer-Tafel pathway and the Volmer-Heyrovski route [44]. For the water to adsorb and subsequently release as molecular hydrogen efficiently, it needs a material with a suiting binding strength.

As stated before, platinum is the best performing catalyst in terms of activity, reaching low overpotentials due to an ideal binding strength. However, platinum is scarce and due to that, extremely expensive (28-30 euro per gram). For large-scale hydrogen production these prices are not favourable. Due to that, there is a demand for cheap, earth-abundant catalysts for the HER. One promising combination of materials is an alloy of nickel and molybdenum.

1.3 Nickel-molybdenum HER catalyst

The Ni-Mo catalyst has been recognised as one of the most promising earth-abundant metal alloys for the hydrogen evolution reaction (HER) in alkaline media [52]. The Ni-Mo combination reaches low over-potentials [47], [53] and is created with relatively cheap methods and materials. [41], [54]. Recently, the group of J. Zhang et al [55] even proved that a Ni-Mo alloy, combined with MoO_2 composites, could perform better than platinum per geometric surface area, with a lower current on-set and a lower overpotential.

The mechanism for the high activity of Ni-Mo is still a point of discussion as J. McKome et al. [56] summarises. Three mechanisms have been proposed here (Figure 6). First is the Sabatier principle where combining a metal that binds hydrogen to strong (nickel) and one that binds to weak (molybdenum) leads to an increase in catalytic activity. The second principle involves a hydrogen spill-over effect where nickel is saturated with hydrogen before it releases over molybdenum. Finally the effect has also been assigned to a very large surface area, which obtains its high activity due to a large amount of catalytically available sites, much like Raney nickel does [21].

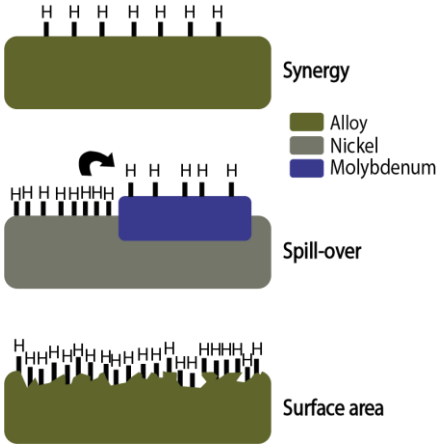

Figure 6. Schematic overview of different mechanisms proposed for the catalytic effectivity of Ni-Mo electrocatalysts

The Ni-Mo catalyst has gathered a lot of attention due to its effectiveness and abundancy. However, the studies around the stability of the catalyst are limited [41], [53], [57]. At high pH's (pH 14 and higher molarities) the molybdenum is known to leach out of the surface [46], [47], [58]. This can reduce the synergy in the alloy and alter the surface composition, which is where catalysis takes place. Furthermore, it is not known how this leaching effects the catalytic processes when performing alkaline water splitting. It was found by J.H.J. Wijten and R. Riemersma [57] how molybdenum first moves from the bulk to the surface of the catalyst. The metallic molybdenum is then oxidised at the surface to molybdate and leaches into the electrolyte solution (Figure 7). Furthermore, in this study they found that KOH and NaOH had different leaching rates and sodium could move into the coating.

The leaching of molybdenum is an oxidative process as the oxidation state of molybdenum is increased from 0 to +6. The fact that this process occurs spontaneously at a negatively charged (reductive) electrode must indicate it has a strong oxidative potential. Stronger than the reductive potential that is being applied on the cathode during experiments. The oxidation mechanism of molybdenum is complex and can take several routes, well described by M. Hull [59] and M. deKay Thompson [60]. While many routes are possible within this mechanism, in alkaline solutions the end product is molybdate (MoO_4^{2-}) and the reaction is always hydroxide concentration stimulated. The half reaction is presented here below.

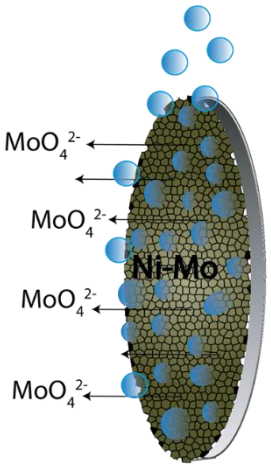

Figure 7. Molybdate leaching from Ni-Mo electrode during electrocatalysis

As this leaching effect is happening at the surface of the Ni-Mo electrode, it is of interest to see how the catalyst changes its behaviour when these changes take place. Does it lose its synergy or spill-over effect, or does it perform better when pores remain after leaching. Furthermore, it is not clear what the influences of the electrolytes are on this leaching process. Harsh conditions (industrial) for the HER are found in the chlor-alkali process at 60-90^{0}C in 6-9M KOH [45], [61], [62]. Standard laboratory testing conditions are at 25^{0}C in 0.1-1M NaOH/KOH [41], [63]. Other cations and lower hydroxide concentration are rarely reported for the Ni-Mo catalyst [64].

Research goal

The goal of this research is to obtain detailed information about the behaviour and stability of the Ni-Mo electrocatalyst when influenced by a difference in pH and cationic electrolytes during the hydrogen evolution reaction. The process of molybdenum leaching out the catalytic alloy and its effects on the catalysis will be the main focus of this study. By studying the processes happening at the surface of the Ni-Mo catalyst a deeper knowledge can be obtained about the processes surrounding this electrocatalyst.

2. Methodology

2.1 Synthesis

In this study the HER active Ni-Mo alloy coatings were applied on titanium stubs using electrodeposition. Titanium was used as a substrate for the coating as it exhibits low catalytic activity towards the hydrogen evolution reaction [65] and has high stability in alkaline solutions [31]. The titanium stub is designed to be mountable into an electrochemical cell, but also usable in several analysis techniques such as scanning electron microscopy (SEM) with energy dispersive x-ray spectroscopy (EDX) and X-ray diffraction (XRD). The titanium stub has a geometric surface area of around 1.256 cm^2. A schematic of the titanium stub is displayed in Figure 8. After the synthesis via electrodeposition, the Ni-Mo alloy is used as catalyst for the HER. The catalysts are analysed using several techniques which are elaborated in sections 2.2. to 2.4.

2.1.1 Electrodeposition

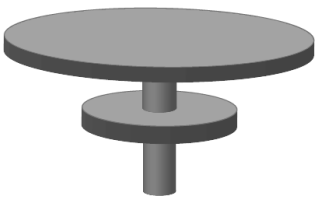

Figure 8 schematic of the titanium stub used as a substrate for the Ni-Mo coating.

Electrodeposition is the technique used in this study to apply the Ni-Mo alloy on the titanium stubs. Electrodeposition requires a relatively easy set-up of a metal-salts bath combined with a potentiostat and two electrodes. Using induced co-deposition the Ni-Mo alloy was coated onto the top-surface of the titanium stub shown in Figure 8. Induced co-deposition is a way in which some bi-metallic alloys can be obtained in relatively easier ways than using metallurgical processes [41]. It is easier in a practical sense, using a simple set up of a metal-salts solution bath at room temperature, in which a to-be-coated conductive substrate is placed. Using a potentiostat, a potential difference is applied until a current starts to flow and deposition occurs at the surface of the electrode. The theoretical aspects of electrodeposition involves a large amount of thermodynamics and complicated reaction pathways which is not within the scope of this thesis, but is well explained in '*Electrodeposition and Surface Finishing* [66]'. For the Ni-Mo alloy *Podlaha and Landolt* [67]–[69] proposed a pathway in which sodium citrate plays a crucial role for the co-deposition of molybdenum. That reaction pathway is presented below.

$$[Ni(C_6H_5O_7)]^- + 2\,e^- \rightarrow Ni(s) + (C_6H_5O_7)^{3-}$$

$$MoO_4^{2-} + [Ni(C_6H_5O_7)]^- + 2\,H_2O + 2\,e^- \rightarrow [Ni(C_6H_5O_7)MoO_2]_{ads}^- + 4\,OH^-$$

$$[Ni(C_6H_5O_7)MoO_2]_{ads}^- + 2\,H_2O + 4\,e^- \rightarrow Mo(s) + [Ni(C_6H_5O_7)]^- + 4\,OH^-$$

In this mechanism, citrate plays a catalytic role where it aids in both the adsorption and reduction of both metals by forming a complex with them during deposition.
The top of the titanium substrate was polished before deposition using 500, 1200 and 4000 grid silicon carbide abrasion paper, so that a smooth surface was obtained. The substrates were washed three times in an ultra-sonificator for 20 minutes, first using a 50:50 ethanol/acetone mixture to remove organics, thereafter in a 2 M nitric acid solution to remove inorganics, and finally in demineralized water to remove residuals from the previous two steps.
The metal-salt solution was prepared using 30 mM Ni(II)SO_4· 6 H_2O (≥99%), 30 mM $Na_3(C_6H_5O_7)$·2 H2O (sodium citrate ≥99%) and 20mM Na_2MoO_4· 2 H_2O (≥99.5%). 100 mL demi-water was added and the pH adjusted to ~10 using NH_3 (28-30%, 2-3 mL). The solution was subsequently added to the electrochemical cell and stirred for 15 minutes at 400 rpm. The cell was then flushed with argon for 20 minutes to remove all dissolved oxygen before deposition.
The cleaned titanium substrates were then carefully mounted into the electrochemical cell as the working electrode (see Figure 9). A copper rod was used to provide a conducting support for the titanium stub. The copper rod was mounted in a glass tube to prevent contact with the solution. Using Teflon-tape, the titanium stub in the glass rod was covered in such a way that only the top-surface of the titanium could be coated. A platinum grid was positioned at approximately 3 cm from the working electrode to serve as a counter electrode.
Using the Ivium Compactstat. h (potentiostat) a steady -100 mA current was applied using transient chrono-potentiometry for 20 minutes under constant 400 rpm stirring. After the deposition the titanium substrates were removed from the solution and rinsed with demi-water. Samples were dried in air and stored before use in electro-catalysis.

Figure 9. 1) titanium stub 2) copper rod 3) glass tube 4) Final electrode covered with Teflon tape

2.2 Electro-catalysis

Electro-catalysis is performed on the Ni-Mo alloys as the means to perform the splitting of water through electrolysis. Before, after and during electro-catalysis, electrochemical analysis techniques were performed to gain information about the catalyst's stability and performance. The electro-catalysis was performed in a three-electrode set-up electrochemical cell, consisting of a working electrode (WE), counter electrode (CE) and reference electrode (RE). The reference electrode is an Ag/AgCl electrode (3M KCl) with a known potential of +0.210 V (vs. RHE). For the counter electrode (anode) a pure platinum grid was used. Platinum is not the best material for the OER due to a high resistance oxide/hydroxide film on its surface which forms at those potentials. However this oxide film does not easily corrode further so offers long-term stability in alkaline solutions [34] [50].
The electrodeposited Ni-Mo alloys on titanium stubs were used as the working electrode (cathode). As the Ni-Mo serves as the catalyst for the HER, its surface is where the reduction from water to hydrogen occurs.

Before the electrodes were mounted into the electrochemical cell, an electrolyte solution was prepared for catalysis. This electrolyte solution is the main substance that has been changed throughout this research thesis. Both the cations and anions were varied to observe changes in the stability of the Ni-Mo electrocatalyst. The anion of interest is the hydroxide-ion (OH^-) as it serves as a reactant for the OER and as a conductive electrolyte in the cell. The concentration of hydroxide-ions is varied between 10^{-6} M and 6 M. When hydroxide concentrations below 1 M were used, additional electrolytes in the form of $(Na_2/K_2/Li_2)SO_4$ were added to ensure conduction of the solution.
The cation M, used as electrolyte salt, was varied between Li, Na and K in their highest purity hydroxide forms. When aiming for hydroxide concentrations of below 1M, their sulphate substituents (M_2SO_4 ≥99%) were used to keep concentrations stable. Other cations such as earth alkali metals were looked into, but did not meet the solubility requirement of at least one mole per litre.

Table 1. Anion and cation variations for all tested samples. Every variation has been employed in duplo and all samples performed electro-catalysis for 72 hours (3 days).

Sample	**Cation**	**(Cation)•OH concentration**	**pH**	**Additional: $(Cation)_2$•Sulphate**
		M	**-log(H^+)**	**M**
JD01	Sodium	1.00	14	0.00
JD02	Sodium	1.00	14	0.00
JD03	Sodium	1.00×10^{-2}	12	3.26×10^{-1}
JD04	Sodium	1.00×10^{-2}	12	3.26×10^{-1}
JD05	Sodium	1.00×10^{-4}	10	3.33×10^{-1}
JD06	Sodium	1.00×10^{-4}	10	3.33×10^{-1}
JD07	Sodium	1.00×10^{-6}	8	3.33×10^{-1}
JD08	Sodium	1.00×10^{-6}	8	3.33×10^{-1}
JD09	Sodium	6.00	14.8	0.00
JD10	Sodium	6.00	14.8	0.00
JD11	Potassium	1.00	14	0.00
JD12	Potassium	1.00	14	0.00
JD13	Potassium	1.00×10^{-2}	12	3.26×10^{-1}
JD14	Potassium	1.00×10^{-2}	12	3.26×10^{-1}
JD15	Potassium	1.00×10^{-4}	10	3.33×10^{-1}
JD16	Potassium	1.00×10^{-4}	10	3.33×10^{-1}
JD17	Potassium	1.00×10^{-6}	8	3.33×10^{-1}
JD18	Potassium	1.00×10^{-6}	8	3.33×10^{-1}
JD19	Potassium	6.00	14.8	0.00
JD20	Potassium	6.00	14.8	0.00
JD21	Lithium	1.00	14	0.00
JD22	Lithium	1.00	14	0.00
JD23	Lithium	1.00×10^{-2}	12	3.26×10^{-1}
JD24	Lithium	1.00×10^{-2}	12	3.26×10^{-1}
JD25	Lithium	1.00×10^{-4}	10	3.33×10^{-1}
JD26	Lithium	1.00×10^{-4}	10	3.33×10^{-1}
JD27	Lithium	1.00×10^{-6}	8	3.33×10^{-1}
JD28	Lithium	1.00×10^{-6}	8	3.33×10^{-1}

In Table 1 the different variations used per sample, are presented in a clear overview. All variations have been performed in duplo as a way to observe differences between samples and to compare when artefacts are observed. Catalysis with 6 M LiOH was not possible as the solubility of lithium is not high enough. All catalysis were performed for 72 h.

Electrolyte solutions were prepared in 200 mL volumetric flasks according to Table 1. From each electrolyte solution that was prepared, a 10 mL sample was taken for quantitative ICP-AES analysis. After sampling, the remaining solution was transferred into the electrochemical cell. This cell is able to contain about 100-150 mL of solution and was filled with approximately 125 mL. The cell was subsequently deoxygenated for 20 min by Ar bubbling. After transferring the solution into the cell, the electrodes were prepared to be used.
The Ag/AgCl reference electrode was thoroughly rinsed with demi-water to remove any residual KCl that could contaminate the electrolyte solution. A butane flame was used for several seconds (until red-hot) to burn contaminants from the platinum counter electrode. The working electrode was prepared in a similar way as was performed for electrodeposition. The entire titanium stub, except for its top-surface was covered with Teflon-tape so that only the Ni-Mo coated alloy was exposed to the electrolyte solution. After preparations the electrodes were mounted into the cell and connected to the Ivium potentiostat for catalysis.
Electrocatalysis was performed at current density of -10 mA/cm^2 using the 'transient chrono-potentiometry' mode via the Ivium potentiostat software. This technique will be further elaborated in section 2.3.1. As the titanium stub surface is about 1.256 cm^2, the applied current on the catalyst was -12.56 mA.

2.3 Electrochemical analysis techniques

Before, during and after catalysis several electrochemical analysis techniques were performed to analyse the stability and performance of the electrocatalyst in detail. Three types of electrochemical techniques were used: 1) Transient chrono-potentiometry for catalysis and overpotential analysis, 2) Cyclic Voltammetry for double-layer capacitance and surface roughening of the catalyst, 3) Linear Sweep Voltammetry for the performance (current) of the catalyst over a certain overpotential range. These techniques are all performed subsequently in one batch-mode, in a single electrochemical cell. First a cyclic voltammogram was taken, followed up by a linear sweep scan. Then catalysis was performed for 72 h with a cyclic voltammogram and linear sweep scan directly after. The different techniques are explained in detail in the sub-paragraphs below.

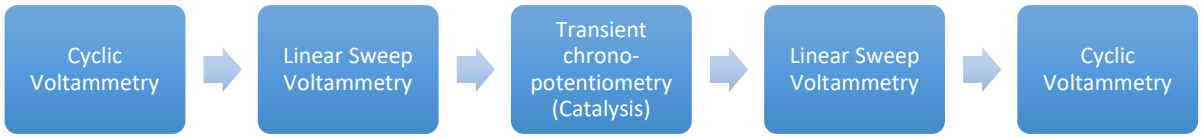

2.3.1 Transient chrono-potentiometry

Using transient chrono-potentiometry, a current is kept constant during a redox reaction using a potentiostat. The potential needed to maintain this redox-current is variable and is recorded over time. The amount of potential needed to maintain the set current signifies the efficiency of the reaction and stability of the electrode. As current times potential equals power, a lower power needed for a reaction equals a higher efficiency. An increase in absolute applied potential means system resistances have gone up, due to for example reactants running out or electrode performance decreasing. To accredit one (or a combination) of these to the decrease in efficiency, requires careful understanding and control of the system and the reactions taking place.

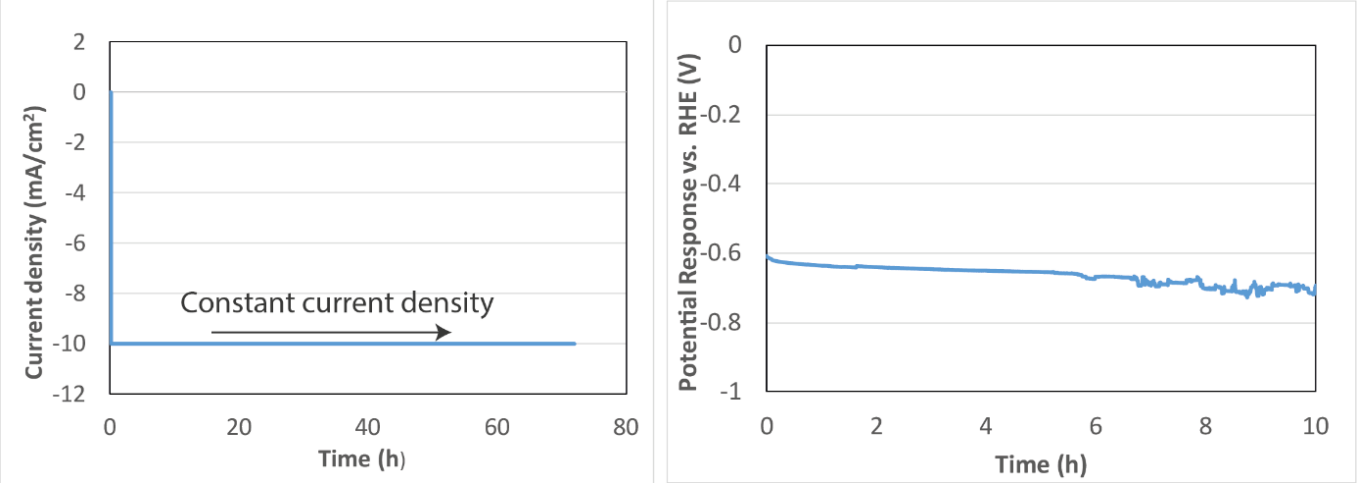

Figure 10. A) The action performed by the potentiostat of applying a current on the electrodes, that is being kept steady for a set duration. B) The response measured by the potentiostat of a variable potential needed to keep the current steady.

An overview for how transient chrono-potentiometry works is presented in Figure 10A and B. Figure 10A displays how an applied current is being kept constant over time. Figure 10B shows how the potential varies to keep the current stable over time and which is recorded by the Ivium potentiostat.

During catalysis the potential changes were analysed by looking at the overpotential (η) needed to maintain a current density of -10 mA/cm². By tracking the overpotential changes using transient chrono-potentiometry, the catalyst its efficiency during catalysis was studied. By using the three-electrode system only the overpotential changes at the Ni-Mo electrocatalyst were analysed. Catalysis was performed for 72 h per catalyst, which is the timescale on which the catalysts significantly changes and for which leaching is measurable.

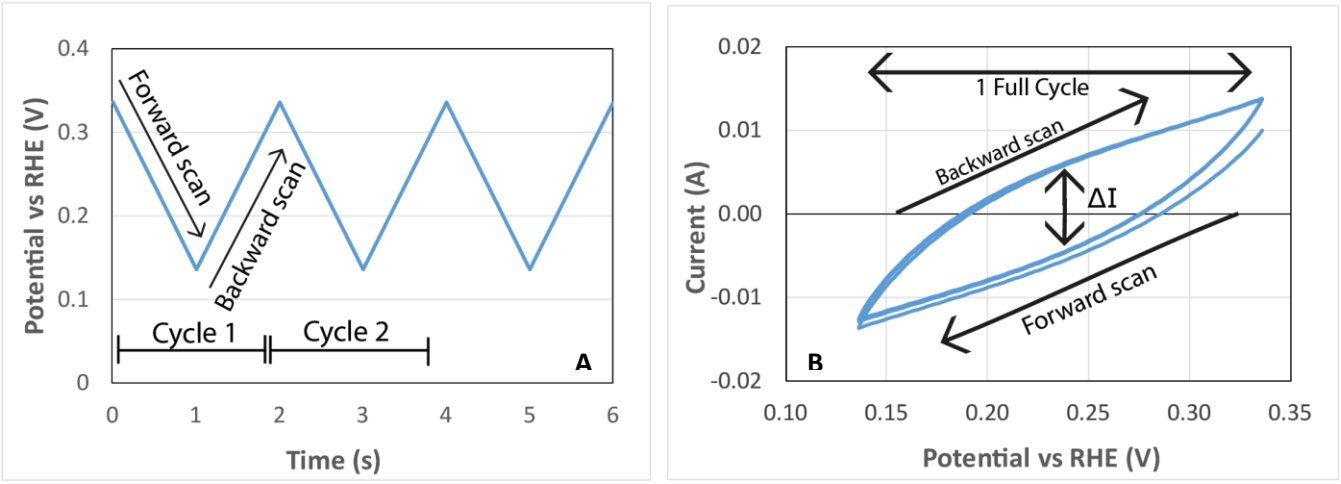

Figure 11. A) The voltage that is applied over time as the scan rate. The scan is performed in a forward and backward direction and can be respeated for multiple cycles. B) The current response when applying the scanrate in a forward and backward direction). The difference between the forward and backward response is used to calculate the capacitance of the electrode.

2.3.2 Cyclic Voltammetry

Theoretical aspect

Cyclic voltammetry (CV) is often used to study electro-chemical behaviour of active species in a solution by scanning over a potential range where redox reactions are present [70], [71]. In this thesis CV is used as the electro-chemical technique to calculate the double-layer capacitance (C_{dl}) at the catalyst surface. In a CV measurement a linear potential change is applied over time of which the slope is called the scan rate (V/s). This scan rate is applied in a forward scan and a backward scan which together form a full cycle (Figure 11a).
The response of a CV measurement is the current that occurs when scanning at a certain rate over the potential range in a full cycle (Figure 11b). The difference in current, between the forward and backward scan is called hysteresis and forms due to the formation of an electric double-layer as described in section 1.2. From this difference the capacitance in Farads can be calculated. The capacitance is linked to the current and potential according to formula 4.

$$Capacitance\ (mF) = \frac{\Delta I(mA) \cdot t(s)}{E(V)} \qquad (Formula\ 4)$$

As the scan rate is in Volts per second and the current-response in Ampere, the slope of the current response is in Farads. To calculate the double-layer capacitance, the difference between the current in the hysteresis (ΔI) at different scan rates is measured and plotted in a graph. Multiple scan rates are measured to reduce any possible errors due to presence of Faradaic current. The slope of the linear correlation between the scan rates and current is the double-layer capacitance of the electrode, i.e. the amount of charge the surface of the electrode can hold.

Experimental

Observed current can either be adsorption of ions, or Faradaic current which flows when a redox reaction is present at that potential range. For proper capacitance measurements only adsorption is of interest and Faradaic events should not take place. Therefore, a non-Faradaic region of 0.2 V between 0.1 and 0.3 V (vs. RHE) was scanned using CV. Three cycles per scan rate were used to get a more accurate average of the difference between the forward and backward scan. Five different scan rates were applied from 0.1 V/s to 0.5 V/s. The CV scan was performed before and after catalysis and the obtained results were used to calculate the change in capacitance.

From the measured capacitances, a roughness factor for each catalyst before and after catalysis was calculated. To calculate this roughness factor a specific capacitance is needed. This, in theory, is the capacitance of a Ni-Mo electrode with a perfect flat surface. However, the value specific for Ni-Mo is not mentioned in literature, so a pure nickel and pure molybdenum electrode were created. These electrodes were polished and then measured for their capacitance using CV.
It should be noted that the polishing of the molybdenum electrode was difficult, as the material was very brittle. A flat, shining surface (which was obtained for nickel) was impossible to obtain without damaging the electrode. A consequence of this, is possible higher capacitance values for molybdenum, which should be taken into account when calculating the roughness factor. After measuring the capacitances, they were combined in the desired ratio to obtain the specific capacitance for a Ni-Mo electrode.

$$Roughness\ factor\ (Rf) = \frac{(C_{dl}/A)}{C_s} \quad (Formula\ 5)$$

Formula 5 is used for the calculation of the roughness factor of the electrocatalysts. C_{dl} is the measured capacitance of the electrode in mF. A is the electrode surface area in cm^2 and finally C_s the specific capacitance in mF/cm^2. The effect of catalysis on the roughness is compared for the different parameters which gives an indication for the electrolyte effects on the change in surface roughness of the electrocatalyst.

2.3.3 Linear Sweep Voltammetry

Linear sweep voltammetry (LSV) is the technique used to see the selectivity for the HER. In a LSV measurement a linear potential change over time is applied. However, only in one direction and over a longer scan range. Information that can be obtained using this technique is if any side reactions are taking place over the scan range. Extra current and changes in the slope will be observed for side reactions. Reduction of oxidized species, or maybe even leaching can all produce current over a potential range, which will be observed in a LSV curve. Furthermore, it gives extra information at what potential the current starts flowing (overpotential) and how strong, although transient chrono-potentiometry can be used for this as well. An electrode that produces the largest current at a certain potential, is the most efficient for its reaction. In this thesis the efficiency for the HER at the cathode is measured which starts at a overpotential of 0 V (vs RHE). From this starting potential an overpotential towards -0.6 V is applied with a scan rate of 5 mV/s.

2.4 Characterisation and measurements

The catalysts and electrolyte solutions have been characterized using several techniques to obtain information on the catalyst its stability. Morphology and composition were analysed using Scanning electron microscopy and Energy Dispersive X-ray spectroscopy before and after catalysis. Liquid AFM was performed to observe changes in the surface real-time and to prepare for *in-situ* liquid AFM, where electrolysis of water and AFM are performed in series. The electrolyte solutions were analysed for leached ionic species using inductive coupled plasma atomic emission spectroscopy (ICP-EAS).

2.4.1 Scanning electron microscopy - Energy Dispersive X-ray spectroscopy

SEM was used to observe visual changes in the catalyst surface after catalysis of 72 h. Carefully picking recognizable spots on the surface of the catalyst, made it possible to scan the same locations before and after catalysis. Image were taken with horizontal field widths of 500 μm, 400 μm, 100 μm, 20 μm, 10 μm, 2 μm and 500 nm.
The elemental composition of the catalytic alloy was determined using EDX. Using the Oxford Instruments software, the intensity of the spectra was used to determine the ratio between nickel and molybdenum. By subsequently looking at the ratio after catalysis, the change in surface composition was calculated.
Scanning electron microscopy (SEM) with energy dispersive X-ray (EDX) spectroscopy was performed on a FEI Helios Nanolab 600 DualBeam with an Oxford instruments Silicon Drift Detector X-Max energy dispersive spectroscope. EDX mapping was performed with an electron beam of 15 kV and 0.8 nA. All SEM imaging was done using secondary electrons at 15 kV and 0.8 nA.

2.4.2 Inductive Coupled Plasma Atomic Emission Spectroscopy

Inductive Coupled Plasma Atomic Emission Spectroscopy (ICP-AES) is the technique used to determine the composition and quantity of the electrolytes in solution. ICP-AES uses inductively generated plasma to excite single atoms, which subsequently emit characteristic spectral lines of its element. The total intensity corresponds to the concentration of emitting atoms so determines both its composition as its quantity. One disadvantage of this technique is that it is not able to determine the oxidation states of the elements and only gives information about the identity and quantity of ions in solution.
ICP-AES was performed on the samples taken from the electrolyte solution (section 2.2) before and after catalysis. If during catalysis components leach from the catalyst's surface, they should be detectable in the electrolyte solution as the detection limit is around 0.1 mg/L. This makes ICP an ideal candidate for detecting the composition and quantity of leached substances. From each experiment 10 mL samples of electrolyte solutions were collected and acidified to a concentration of 2% HNO_3. Acidified samples were then sent to TNO (Dutch scientific research organisation) where the measurements were performed. ICP-AES was performed for the detection of copper, lithium, sodium, potassium, molybdenum, nickel and titanium traces. Nickel, molybdenum and titanium were analysed as these are the three metals of which the

catalyst is made. Lithium, sodium and potassium as they were used as the electrolytes. Copper was analysed as a copper rod was used to provide a conducting support for the titanium stub.

2.4.3 Atomic Force Microscopy

Surface changes in electrolyte solution were studied using liquid-phase Atomic Force Microscopy (AFM). A Bruker Multimode was used in ScanAsyst Peakforce mode for in-fluid sample analysis, using a silicon nitride (SiN_3) probe. A SiN_3 cantilever was selected due to their high stability in alkaline solutions.
The goal of this liquid-phase AFM is to mimic how an electrode surface changes while submerged in alkaline solutions. Since AFM can study surfaces in liquid without damaging them, it is an ideal technique to scan the surface over a longer period of time to observe changes *in-situ* [72]. These experiments are a preliminary study before the electrode will also be connected to a potentiostat and an actual *in-situ* AFM analysis will be performed during electrolysis. The only difference with an actual *in-situ* analysis is that there is no current/potential applied on the electrode when studied.
New Ni-Mo alloys for electrocatalysis were applied on titanium foil instead of stubs. The stubs used in section 2.1 are not suited for AFM analyses due to their shape, so new electrodepositions had to be performed on these plates. Titanium foil (99.6+% pure) with a thickness of 0.25 mm, was used to cut out 1x1 cm plates. Only changes to the electrodeposition were a -100 mA/cm^2 current density applied for 900 s instead of 1200 s. The stirring speed was increased from 400 to 1000 to avoid bubble formation on the plate surface.
The electrodeposited Ni-Mo samples were mounted onto the Bruker AFM using copper tape. A Bruker fluid cell was added on the sample and several drops of electrolyte solution were deposited into the fluid cell. Both a 1 M KOH and 6 M KOH solution was used for the analysis. An area of 10x10 μm was scanned continuously until the electrolyte solution evaporated or when the tip broke down. Single images took about 15-20 min for a full image scan.

2.4.4 Faradaic efficiency – Gas chromatography

The Faradaic effiency was calculated using Gas Chromatography (GC) analysis connected to a H-cell. In the H-cell the OER and HER were separated by a Nafion perfluorinated membrane (Nafion 117, 0.007 inch thick, Sigma Aldrich). For the electrolyte solution a 50 mL 1 M KOH solution was prepared which was divided over both sides of the H-cell. An platinum grid was used for the OER electrode and the Ni-Mo electrode for the HER. The OER side was purged with 2 mL/min N_2 and 0.1 mL/min Kr. The HER side was purged with 2 mL/min Ar and 0.1 mL/min Kr. The OER electrode was employed as the working electrode and the HER electrode as the counter/reference electrode. Water splitting was performed at a current of 4 mA and was maintained for 72 h. A Global Analyzer Solutions Compact GC 4.0 from Interscience was used for the GC measurement. The OER and HER had separate channels connected to the GC. Produced molecular hydrogen was analyzed using a 75 μL sample loop injecting into a 5m.0.53 mm MXT-Q-bond then a 10m.0.53 MXT-Msieve column and detected on a TCD. Oxygen from the OER side was injected via a 50 μL loop through different columns of the same type and analyzed on a separate TCD. The injection was performed once every minute with an delay time off ±10 s for each injection with Kr used as an internal standard.[73]

3. Results

Previous studies show that molybdenum leaches from a Ni-Mo alloy into the electrolyte solution [21], [45]–[47]. According to these studies a Raney nickel can be obtained by leaching out a secondary metal such as aluminium or molybdenum in highly alkaline solutions (1-10M NaOH/KOH). Divisek et al, showed here that molybdenum is removed using this technique to create Raney nickel, but a residual amount of molybdenum is necessary for the alloy to keep its catalytic activity towards the HER.
Furthermore, it is found by Wijten and Riemersma [57] from our group, using X-ray photoelectron spectroscopy (XPS), how molybdenum first migrates from the bulk to the surface before leaching out. During this study, they found indications that potassium ions led to an increase in leaching compared to sodium ions. Moreover, sodium and potassium ions tend to move into the coating during/after molybdenum leaches out.
Both the cationic (K, Na) and anionic (OH^-) electrolytes supposedly play a role in the leaching of molybdenum from the catalytic Ni-Mo alloy. Thus, in this thesis, we study the influence of these ions. The influences of the anions on leaching, are analysed by varying the hydroxide (OH^-) concentration between 6 M and 10^{-6} M (pH 14.8 - 8). Furthermore, we added lithium to the series of cations next to sodium and potassium as electrolyte. As stated in the previous chapter, the Ni-Mo catalyst is studied before, during and after catalysis by using SEM, ICP, EDX-AES and the various electrochemical techniques such as linear-scanning voltammetry, cyclic voltammetry and chrono-potentiometry.

3.1 The Ni-Mo catalytic activity

Before analysing the electrolyte effects on stability and performance of the Ni-Mo electrocatalysts in depth, the improved activity [41], [46], [55] of combining nickel and molybdenum was confirmed versus their mono-metallic counterparts. The overpotential and over-time changes in required potential were studied by performing a 24 h electro-catalysis with a pure nickel, pure molybdenum and a Ni-Mo alloy catalyst. Furthermore, with this experiment the electrodeposited Ni-Mo catalyst is compared with literature [44], [47], [53] for its overpotential and synergetic effects between the two metals. In Figure 12 the 24 h catalysis is presented for pure nickel, pure molybdenum and the combination of those at a current density of -10 mA/cm^2 in 1 M NaOH.

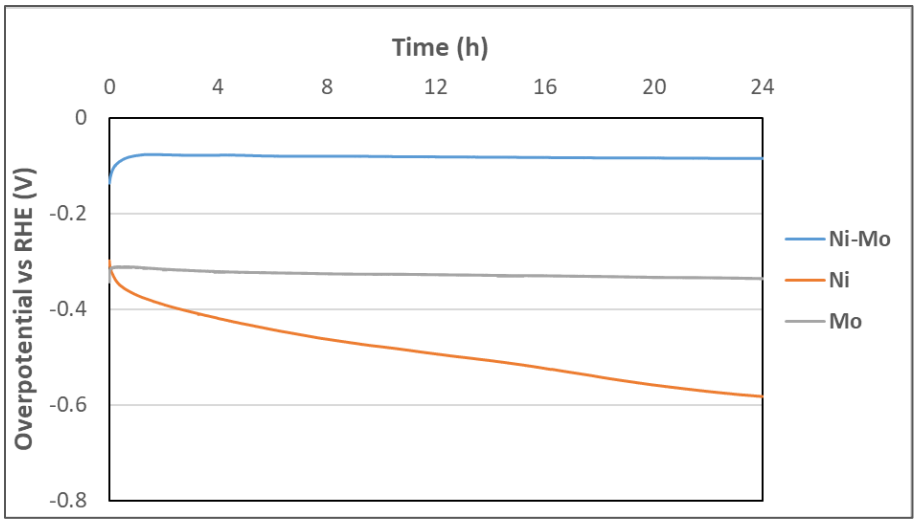

Figure 12. The overpotential needed for the hydrogen evolution reaction at 10 mA/cm² for pure nickel (orange), pure molybdenum (grey) and the alloy of nickel-molybdenum (blue). A clear synergetic effect becomes apparent when combining the two metals into an alloy, greatly reducing the overpotential needed for the reaction to proceed at 10 mA/cm².

Figure 12 displays how combining nickel and molybdenum in an alloy leads to a significant decrease in overpotential for the HER. The obtained overpotential of below -0.1 V is consistent with what is obtained in literature for similar set-ups [44], [47], [53]. The pure nickel catalyst increases in overpotential considerably over the 24 h, which is explained by a nickel poisoning effect where nickel hydrides are formed and catalytic available sites decrease [44], [74]. This effect is no longer visible for the Ni-Mo alloy, which indicates that the combination with molybdenum suppresses the formation of nickel hydrides. This suppression might be explained by the "spill-over effect" [41] mentioned in the introduction, where molybdenum assists in the release of hydrogen due to the weaker binding strength. This experiment shows that the electro-deposited Ni-Mo catalyst for the HER is as efficient as reported in previously mentioned literature. Both the synergetic effects and a significant decrease in overpotential, required for a -10 mA/cm² current density, are evident.

Another effect that was observed in Figure 12, is that the Ni-Mo catalyst has an activation time to reach its lowest overpotential. The overpotential reduces the first hours before it flattens out and becomes 'stable'. This activation time was present in all samples tested in this thesis, however the time varied widely, depending both on the cation and hydroxide concentration used. As a large amount of samples were used for electrocatalysis, an average activation time was calculated from all the transient chrono-potentiometry graphs (for an overview of these graphs see Appendix A). Furthermore, a statistical validated value for the lowest overpotential after activation was determined. These results have been presented in Table 2.

Table 2. Average activation time for each pH variation and cation, with corresponding average lowest overpotential. Measured with transient chrono-potentiometry

	Average activation time (h)			**Overpotential at -10 mA/cm²**
	Li	Na	K	
14.8		5.26	2.74	-99.18 ± 39.19 mV
14	32.2	4.58	5.94	-91.66 ± 14.25 mV
12	22.2	11.42	11.05	-217.09 ± 35.61 mV
10	27.5	11.62	21.3	-298.68 ± 25.89 mV
8	19.45	8.55	13.85	-435.97 ± 26.25 mV

In Table 2 we present the average activation time for each sample variation to reach its minimum overpotential. Additionally, the average minimum overpotential per tested hydroxide concentration was calculated including its standard deviation.
The minimum overpotential changes almost linearly with hydroxide concentration for pH 8 – 14. This effect is explained by the Nernst equation (Formula 3), where the required potential changes as a function of the pH due to a reduction of reactants (OH^-). However, samples at pH 14.8 do not follow this trend, most likely due to an oversaturation of reactants. As the current density is only -10 mA/cm^2, it does not require a concentration higher than 1 M to provide the reactants necessary for water electrolysis. This hypothesis can be confirmed by increasing the current density to where concentration becomes relevant again for propagation of the reaction. This experiment has been performed and will be elaborated in section 3.2.3 – *Current effects*.

We observe large variations in the activation time between the different sample parameters. Two possible causes for this effect can be reasoned. The first explanation is that the Ni-Mo electrode is being chemically reduced back from its oxidised state to wits metallic state. This would explain the reduction in overpotential as more catalytic sites become available in its metallic state [44], [63]. However, this does not explain the big differences between the different cations and hydroxide concentrations. A more reasonable explanation is that the surface area increases, due to leaching of components from the alloy, which reduces the overpotential. This would effectively increase the catalytic surface area, reducing the overpotential needed to maintain the same current. This would also explain why there are such large differences between the parameters, as the parameters are suspected to have an influence on the leaching in the Ni-Mo catalyst. By further researching the properties of leaching and the stability of the Ni-Mo electrocatalyst we aim to explain these observed effects.

3.2 Ni-Mo stability

The stability of the Ni-Mo electrocatalyst was analysed by comparing catalysts and electrolyte solutions before and after catalysis. McCrory et al. [53] devoted a paper to establishing a benchmark for testing the stability of HER and OER catalysts. Within this benchmark they analyse the composition, surface area, extended stability and performance. We used a similar approach, however a longer catalytic stability test (24 vs. 72 h) and a different elemental composition analysis (XPS vs. EDX) is applied, as XPS was already explored in detail by J.H.J Wijten and R. M. Riemersma et al [73].
Within the benchmark, no attention is paid to the electrolyte solution. The electrolyte solution is a valuable source of information to what species leach out the catalyst and how catalysis changes its aqueous environment. In this thesis the electrolyte solution is analysed using ICP-AES, which analyses which atoms and in what concentration are found in the solution.
The first section (3.2.1) focusses on the structural changes in the surface, such as surface roughening and alloy composition changes. The second section (3.2.2) focusses on the electrolyte solution and the leaching of molybdenum from the alloy. In section 3.2.3 the effect of increasing the current density is studied and finally in section 3.2.4 the electrolyte solution is spiked with molybdate to see how it influences the stability.

3.2.1 Structural changes catalyst surface

The stability of the Ni-Mo catalyst surface was studied in detail, as this is where catalysis occurs and where components have the highest mobility to move out the alloy. The surface was studied with SEM-EDX and via capacitance measurements for all electrolyte variations previously mentioned in Table 1 section 2.2. With SEM the surface was analysed for optical changes. EDX aided with the identification of changes in the alloy composition at the surface. Capacitance measurements were performed to calculate a roughness factor that is used as a tool to calculate the change in surface roughness after catalysis.

3.2.1.1 Energy Dispersive X-ray Spectroscopy

The EDX spectra were collected to obtain the atomic composition at the surface of the coating. By analysing the intensity and energy of the spectra, an atomic ratio between nickel and molybdenum on the catalyst surface was determined. After a catalysis time of three days (at -10 mA/cm^2) another spectra of the same surface was measured to analyse how the elemental composition has changed. The change in molybdenum content was calculated from this ratio between Ni and Mo. The results of these calculations for the different electrolyte solutions are presented in Figure 13a-c.

As becomes evident from Figure 13, there is a clear relationship between the pH and the loss in molybdenum content. In the majority of cases, EDX revealed there was a lower loss in molybdenum from the surface present at lower pH. The higher hydroxide concentrations (1-6 M) show the biggest loss in Mo content for all samples. This indicates a concentration dependence for the loss of molybdenum, which is in line with the oxidation mechanism for molybdenum to molybdate.
Furthermore, there clearly is a cation effect present in the loss of molybdenum content from the catalyst. Potassium based electrolyte solutions (Figure 13C) show a far greater loss of molybdenum content after catalysis. Lithium and sodium based electrolyte solutions show roughly equal leaching at lower pH's, while potassium shows higher molybdenum content loss at all pH's.

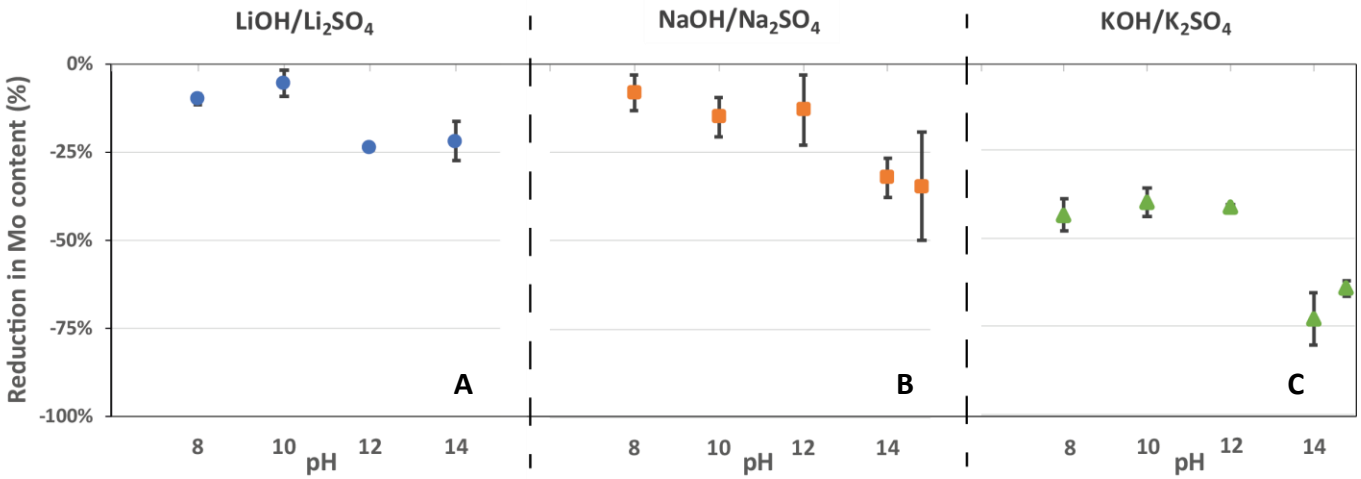

Figure 13. EDX results converted to molybdenum content loss. Each point in the graph represents two samples spent for 72 h at 10 mA/cm^2, each at different hydroxide concentration (10^{-6} M – 6M) and cations (Li, Na and K).

Contrary to the more obvious hypothesis that the hydroxide concentration would play the biggest role for the loss in Mo content, as the oxidation mechanism would suggest, the cations too show an equally large influence. A lithium-based electrolyte solution shows an average loss of 15.3%[1], sodium an average of 20.6% and potassium a striking 47.8%. There are multiple hypothesised explanations for this effect. The most probable is a solubility effect as potassium molybdate is almost twice as soluble as its smaller cation constituents [73]. Another possibility has to do with a shielding effect in the double-layer. As potassium is the largest cation with the lowest charge density of the three studied cations, it could be due to poor charge shielding in the electric double-layer of the electrode. Poor charge shielding would enable a more mobile double layer, which makes leaching from the alloy into the electrolyte solution easier. Lastly, in the previously mentioned XPS study, sodium and lithium were observed to migrate into the alloy in higher contents [73], which could form a complex with molybdate or simply block leaching from the alloy into the solution. Also, it could move into the porosity, left behind by the leaching of molybdenum and essentially blocking the channels for further leaching.

Calculated atomic ratio Ni-Mo

The amount of catalysts synthesized for experiments offer a unique opportunity to calculate a statistical validated value for the ratio between nickel and molybdenum before catalysis from the EDX data. As electro-deposition tends to create alloys that can vary in composition depending on the method, it is of interest what ratio is obtained for the method used in this thesis (section 2.1.1). For this calculation 40 unused catalysts EDX spectra have been collected and the average Ni-Mo content has been determined from that. The results of which are listed in Table *3*.

Table 3. Ratio between nickel and molybdenum calculated from 40 unused Ni-Mo catalysts

	Content (atomic %)
Nickel content	67.39% ±4.21%
Molybdenum content	32.61% ±4.21%

An average 2:1 ratio between nickel and molybdenum was determined, with a relatively low standard deviation. This 2:1 Ni-Mo ratio is in line with reported literature [46], [58]. An important note here is that this analysis and calculation could not distinguish between metallic or oxidized species.

Alloy thickness

Another phenomenon that was observed using EDX, was a widely variating alloy thicknesses between different catalysts. Within samples with thin alloys, a strong titanium peak became visible in the EDX spectra. This observation becomes evident in Figure 14, where SEM images combined with EDX show the surface of the catalyst.

[1] As no catalysis was performed for 6M LiOH (solubility constraints) and pH 14.8 has shown to be the biggest contributor for the loss in molybdenum, the lithium value is lower.

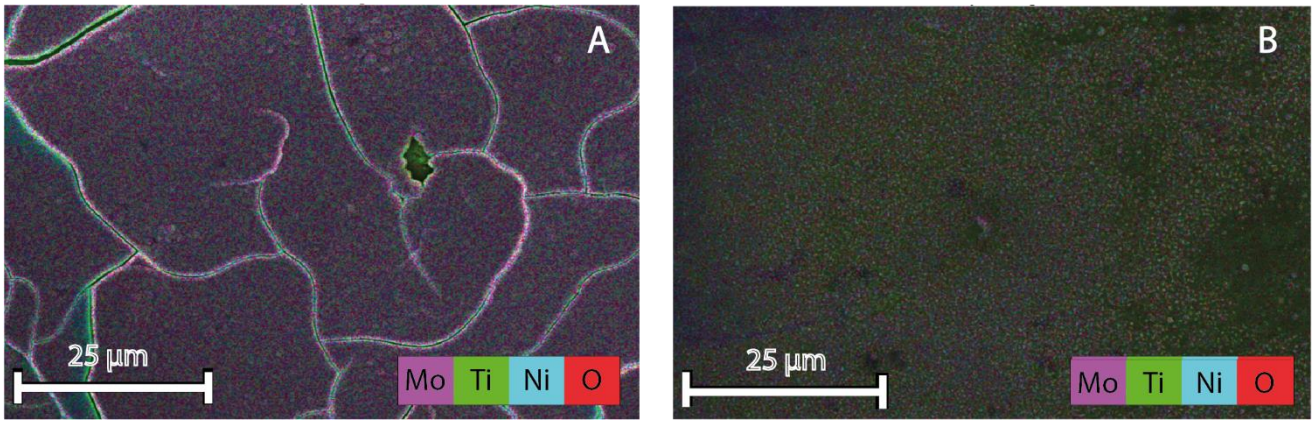

Figure 14. SEM-EDX images of Ni-Mo electrocatalyst surfaces. Both created with the same electrodeposition techniques. 8A displays a thick Ni-Mo coating on the titanium substrate. Fig.8b shows an thin alloy where the titanium shows through the coating itself.

In Figure 14 we compare two Ni-Mo coatings with a large difference in alloy thickness. Figure 14a shows a thick alloy where titanium (in green) has completely been covered with Ni-Mo, except for the small defect that shows the titanium underneath. Figure 14b shows a thin alloy where the substrate is covered with a very thin layer and large amounts of titanium penetrates through. The fact that the coatings can vary this significantly in thickness, suggests that the reproducibility of the catalytic alloys during electrodeposition is low.
It was noticed with the SEM-EDX, that the first synthesized alloys from a new batch showed this thin coating behaviour. After three or four catalysts were synthesized the alloys displayed thicker metallic layers. Furthermore, the nickel-molybdenum salt bath turned darker after a few depositions, indicating a change in the solution. Darker solutions gave thicker coatings during deposition. M.P. Pavlov et al. [79] explained this effect due to different oxidation states of molybdenum becoming present in the solution over time. Reproducibility could be enhanced by finding the right deposition time for fresh batches, before the solution darkens, and subsequently renewing the deposition salt-bath faster. However, improving of the electrodeposition was not within the scope of this thesis, so no attempts were made.
Possible consequences of the thin alloys are differences in performance between catalysts and differences in stability between samples. Furthermore, with different coating thicknesses it should be noted that there could be differences in amounts of leaching, simply because there is more molybdenum that can leach from the alloy.

3.2.1.2 Capacitance and roughness

Obtaining a roughness factor from capacitance is a frequently applied method for determining a (catalytic) surface area of electrodes. In literature the double-layer capacitances (C_{dl}) are either obtained with electrical impedance spectrometry (EIS) [41], [61], [75] or with cyclic voltammetry (CV) [35], [53]. To calculate a roughness factor from C_{dl}, the measured double-layer capacitance per area unit, is divided by the specific capacitance (C_s). As was already mentioned in the methodology, the specific capacitance is a reference of a perfect flat surface, ideally of the same elemental composition of the electrode that is being researched. A perfect flat surface of the same material however, is rarely optional or found in literature. A flat analogous material/reference is then selected for the specific capacitance of which the accuracy is unknown.

However, during this thesis we created two pure nickel and molybdenum electrodes to analyse the Ni-Mo catalytic effect. These electrodes have been polished before use to obtain an as flat as possible surface. Furthermore, using EDX a statistically validated ratio between nickel and molybdenum has been determined. With the use of CV and the EDX ratio, an attempt is made to determine a more accurate specific capacitance. This specific capacitance can then be used for a roughness determination for all tested catalysts. The calculated specific capacitance and the data with which it is calculated is displayed in Table 4.

Table 4. The measured data from CV measurements used to calculate the specific capacitance. The measured capacitance per electrode was divided by the surface area of the electrode (1.257 cm^2) to obtain the capacitance per unit area.

	Capacitance (mF)	mF/ cm^2	ratio	Specific capactiance (mF/cm^2)
Ni	0.176	0.140	67.4%	**7.54**
Mo	28.70	22.83	32.6%	

The specific capacitance was calculated to be 7.54 mF/cm^2. As becomes evident from Table 4, the biggest contributor to the specific capacitance was the pure molybdenum electrode capacitance. As was already mentioned in the methodology, the surface polishing of this electrode was challenging due to the brittleness of the material. As capacitance is a function of the surface area, the high roughness is most likely the biggest contributor to the molybdenum electrode its high value. A 'real' value for the specific capacitance would in theory be several factors lower, somewhere in line with the nickel electrode.
A specific capacitance for an alloy like we use in this thesis will always be an estimation. Specific capacitance is material specific, which means nickel and molybdenum both have their own specific capacitance as a flat metal surface. In an alloy both nickel and molybdenum are mixed in a ratio and as we have already seen with EDX, the end composition of the alloy can change during catalysis due to leaching. This means the specific capacitance would need to be altered for each change in ratio, which makes accurate estimation difficult. Another variable that can change the specific capacitance is the amount of oxidized species at the surface. As the surface becomes oxidized when no reductive potential is applied, the surface can hold less charge. All these variables make the specific capacitance an almost unreachable value to which an estimation should suffice.

In literature a value between 20 and 40 μF/cm^2 is used several times for 'similar' electrodes [41], [45], [53], [61], [75]. The value calculated by our method lies several factors higher, but will be used as a reference surface/capacitance due to the material and ratio combination. Since we are comparing roughness before and after catalysis the change in the roughness factor is of higher significance than the height of the factor itself. The percentage increase in the roughness factor compared to the before measured roughness factor, will hereafter be referred to as the 'Roughness Factor Increase' (RFI).
Even though the determined specific capacitance value is high, it has been used to compare the Ni-Mo electrocatalysts before and after catalysis. The capacitance values were determined from the CV data using the method described in the methodology. These capacitance values were subsequently converted to roughness factors via formula 5. The roughness factors are sorted for their cation constituents and plotted versus their pH influence. In Figure 15 the different roughness factors for all variations are displayed.

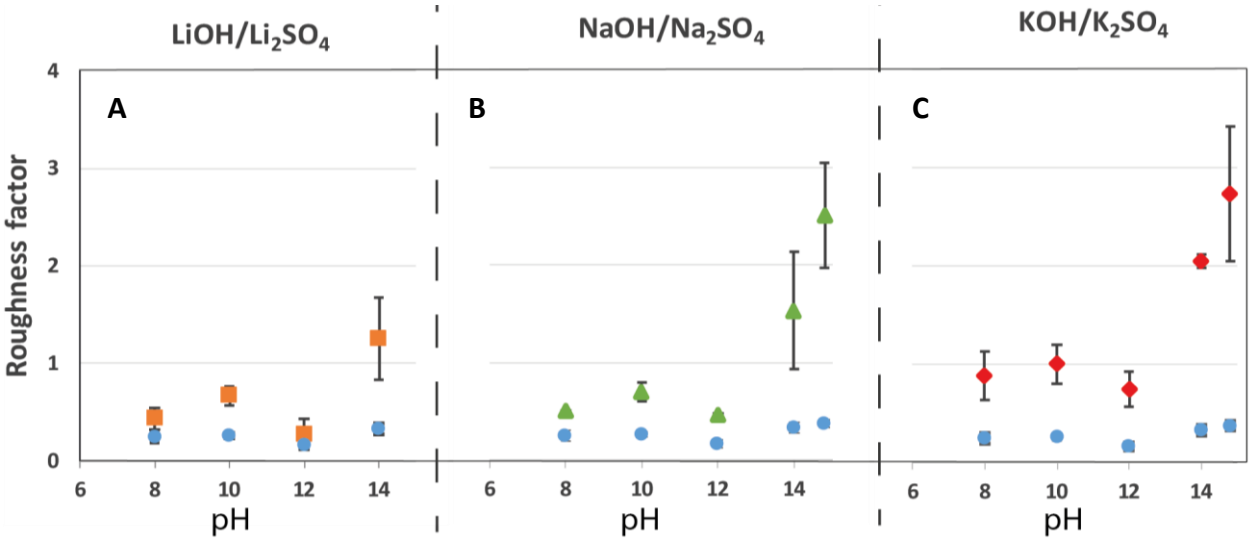

Figure 15. The roughness factors before (blue) and after 72 h catalysis at -10 mA/cm², per cation (Li, Na, K) at different pH levels. Each point represents two experiments with the error displayed in bars between the two experiments.

Figure 15A-C both show the roughness factor before catalysis (blue) and after 72 h of catalysis. It becomes apparent that the roughness factor follows the same trends as the EDX spectra indicated. As the hydroxide concentration increased from pH 8 to 14.8, the surface roughness increases correspondingly. The highest roughness factors are observed at pH 14 and pH 14.8 further confirming that the hydroxide concentrations plays a significant role in the changing of the catalyst surface. Furthermore, it can be observed that the cation-effect pattern is essentially the same, with potassium (Figure 15C) obtaining the highest roughness factor after catalysis. When plotting the cations versus the RFI due to catalysis, the cations influence becomes even more evident (see Figure 16)

A steep increase in Figure 16 from sodium to potassium for all pH levels indicate the far stronger surface roughening when using potassium-based electrolyte solutions. A particularly interesting fact in this graph is that it shows there is a minimum in roughening around pH 12. Especially with lithium, but also with sodium, the RFI values are significantly lower. For lithium the value at pH 12 shows even lower surface roughening than lower hydroxide concentrations.

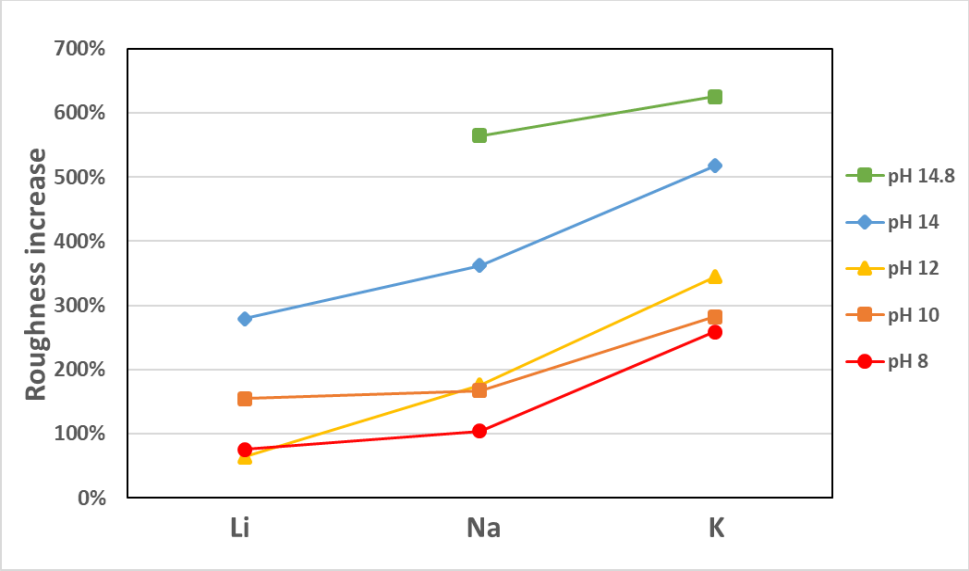

Figure 16. Caculated surface roughness increases (RFI) after catalysis plotted vs the cation used in the electrolyte solution. A RFI of 0% represents no change in roughness factor.

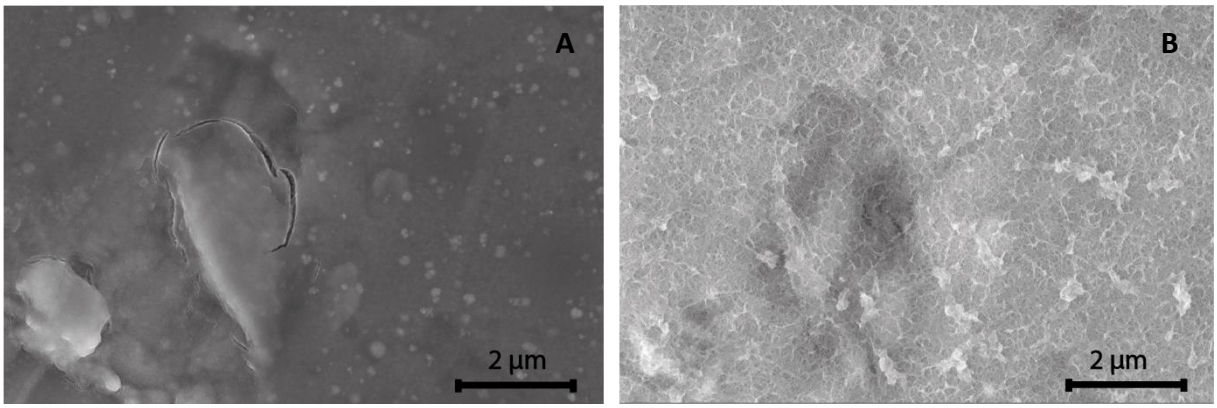

Figure 17 SEM images at the same location before and after catalysis. A) a relative flat Ni-Mo surface with a single crack visible. B) An altered surface after catalysis showing a high surface roughening and a web like structure

By applying SEM on sample JD19 (potassium - pH 14.8) the strong effect of surface roughening became visually apparent. Figure 17 shows the surface of the Ni-Mo electrode before (17A) and after catalysis (Figure 17B) at the exact same location. The SEM images display a flat surface before the catalysis with some minor cracks, while after catalysis the entire surface has altered into a web-like structure with a far larger surface area. This effect was evident in almost all samples, especially at higher hydroxide concentration, as can be observed in Appendix B.

With the supporting evidence of the SEM and EDX measurements, the high roughness factors that were calculated from capacitance measurements can be ascribed to the reduction of molybdenum from the surface. The reduction of molybdenum content from the surface of the catalyst follows the exact trend as the increase in in surface roughness. This became most apparent when molybdenum leached the strongest at higher hydroxide concentrations and as the atomic number of the cation increased.

3.2.2 Electrolyte solution changes

In the previous section we focussed on how the catalyst its surface changes in both roughness and composition during catalysis. This section primarily focusses on the changes in the electrolyte solution to study the stability. As mentioned previously, the molybdenum leaches from the surface of the catalyst in the electrolyte solution as the anionic molybdate. ICP-AES is able to detect concentrations starting at 0.1 mg/L, which should be enough to observe leached ions in the electrolyte solution.

3.2.2.1 Inductive coupled plasma – Atomic emission spectroscopy

With the use of ICP-AES the types and amounts of electrolytes in the solution were analysed in detail. As components leach from the Ni-Mo catalyst surface, they naturally end up in the solution. As mentioned in the methodology, a wide range of species were analysed with ICP-AES. In this section we present the figures for molybdenum and nickel leaching. As the main changes were observed in these two elements, these were worked out in graph form. The list of all other electrolytes found in the electrolyte solution, are presented in Appendix C. The ICP results for molybdenum have been presented in Figure 18.

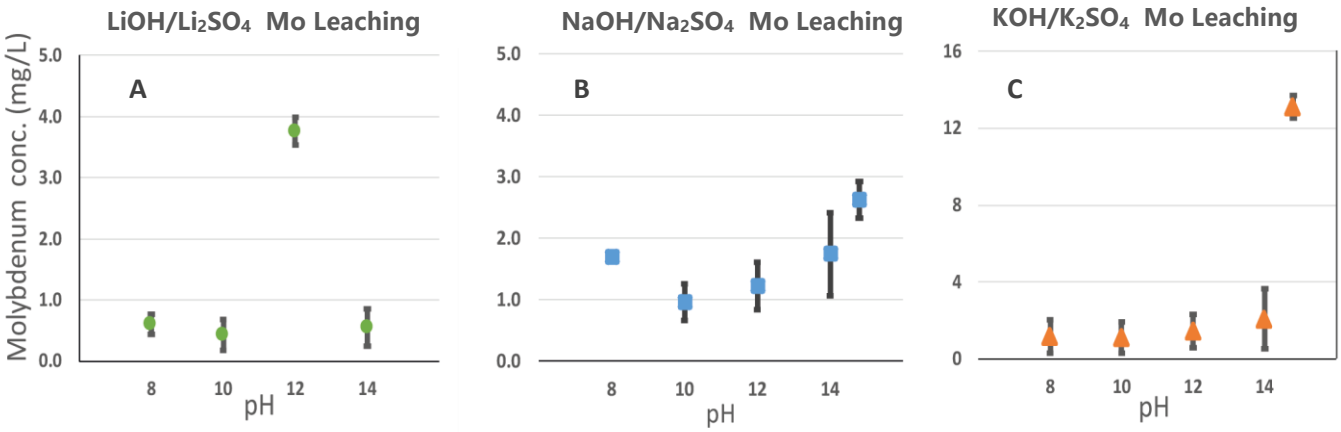

Figure 18. Amounts of molybdenum detected in electrolyte solutions after catalysis using ICP-AES.

In Figure 18 we see the amounts of molybdenum leached from the catalyst in the electrolyte solution in mg/L. In this figure a different graph for each cation was produced with the pH on the X-axis. It is important to note here that potassium has higher values on the Y-axis due to the far higher amount of detected molybdenum at pH 14.8.
Within Figure 18 there is a trend observable for sodium and potassium. In both Figure 18B and Figure 18C we see that at higher pH's more molybdenum ends up in the electrolyte solution. Especially for potassium at pH 14.8, there is an extremely high amount of molybdenum detected in the electrolyte solution of several factors higher than all other samples. This value however, is not surprising as both within the EDX and the capacitance measurements the highest change at the surface was observed for potassium at pH 14.8. As with the other experiments, all results are displayed as duplos, where an average was determined with an error between the two samples. The errors between the samples were often large.
Within the lithium series (Figure 18A) there is no clear trend to be observed. At pH 12 a large amount of molybdenum was detected. However, at this pH for lithium the lowest amount of surface roughening was present from capacitance measurements. There was a slight higher amount of molybdenum leached seen in the lithium series EDX spectra, although this should not explain this significant increase seen here.

A possible explanation for this artefact and also for the present error between duplos, is a difference in alloy thickness. As alloys were observed to have wide varying thicknesses, this could explain to why larger amounts could leach between samples. Another explanation is within the adhesion of the alloy. It was often observed that the edges of the catalyst could be quite brittle and sometimes parts of the catalyst would fall off during hydrogen production. Electrolysis of water produces bubbles, which can cause a strain on the looser parts of the alloy, leading to parts falling off. Care was taken not to transfer these parts in to the sampling bottles, so the likelihood of detecting them is low. However, these parts can be detected with ICP-AES if present, and cause spikes in detected values. The spike seen at lithium pH 12 could also simply be 'lithium leaching behaviour' for which further research would be needed.

Previous results from EDX, capacitance measurements and now ICP-AES would suggest the lowest pH's obtain the highest stability for the catalyst. However, this would only be valid for the stability of molybdenum in the alloy. This becomes visible when we look at the ICP-AES results for nickel in Figure 19.

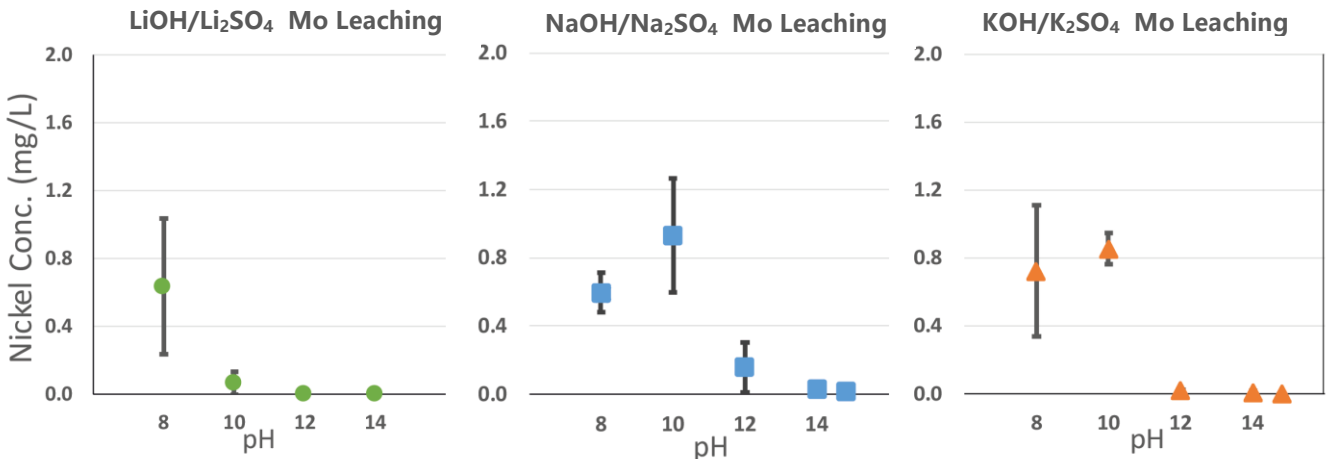

Figure 19. Amount of nickel detected in electrolyte solutions after catalysis of 3 days using ICP-AES.

Figure 19 shows the amount of nickel detected in the electrolyte solutions after catalysis. Here it becomes visible that where molybdenum is being stabilized below pH 12, the nickel loses its stability and starts leaching from the catalyst. As the solution becomes less alkaline, more nickel is detected in the solution. All electrolyte solutions show the same trend, with no large differences between the different cations.

Nickel in alkaline electrolytes is known for its passivating effect where an insoluble hydroxide film forms on the surface of the nickel [31]. Above pH 10 a layer of $Ni(OH)_2$ is formed which has been observed to partially deprotonate to Ni(OOH) [76]. These layers protect the underlaying metal from further corrosion and dissolution. This effect is the reason why the nickel in the previously mentioned Raney alloys survives the etching in strong alkali solutions and obtain their high surface area.

Figure 19 gives an explanation to why there was a minimum in roughness increase around pH 12 observed with the capacitance measurements. This pH appears to be a more stable region, as little to no nickel leaches at this pH and molybdenum does not leach as strong as at pH 14 and 14.8.

3.2.3 Current effects

The leaching of molybdenum is an oxidative process as the amount of electrons of molybdenum is being reduced. The fact that this process occurs spontaneously at a negatively charged electrode must indicate it has sufficiently high oxidative potential that can overcome the reductive surrounding. However, all electro-catalyses have been performed at a current density of only -10 mA/cm^2 that requires a relative low overpotential (± -100mV). This means the reductive potential area around the HER electrode is relatively low. In the following experiment a current density of -500 mA/cm^2 was applied on the electrode, which significantly increases the overpotential needed to maintain it. The cathode has thus become far more negatively charged due to the increased overpotential, which could decrease the oxidative process of molybdenum leaching.

The experiment was performed at a pH of 14 and 14.8 KOH to see if it reduces the amount of molybdenum leached from the alloy after a catalysis time of 72 h. EDX and capacitance were measured before and after catalysis and these results were compared to the results found in previous sections.

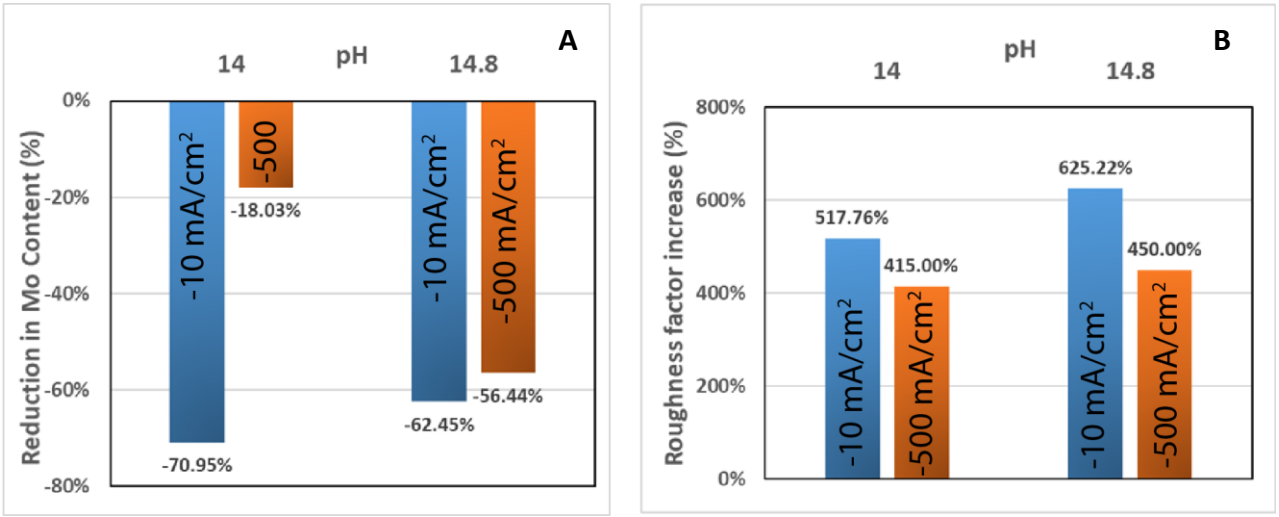

Figure 20. A) EDX analysis of molybdenum content loss at -500 mA/cm² for pH 14 and pH 14.8, compared with the low current density averages from previous sections. B) Capacitance roughness factor increase comparison of high current density vs low current density for pH 14 and 14.8

In Figure 20A we present the EDX measured reduction in molybdenum content, that was compared to the low current density experiments for pH 14 and 14.8. Figure 20B shows the change in roughness factors after catalysis compared to their average lower current density counterparts. In Figure 20A we see how applying a higher current density greatly affects the reduction of molybdenum. Especially for pH 14 there is a far lower amount of molybdenum that was reduced from the alloy surface (18% vs 71%). At pH 14.8 the reduction of molybdenum content is less evident and would fall within the sample error. pH 14.8 (6 M KOH) is most likely still too strongly alkaline to contest with the high current density, as there is still a large reduction in molybdenum present.
A similar trend to EDX is visible for the RFI in Figure 20B, as the high current density leads to lower RFI for both tested samples. A lower RFI was suspected for the high current density pH 14 sample, since EDX showed a low molybdenum content loss. It appears RFI here is not a direct function of the reduction in molybdenum. As stated before capacitance is also influenced by composition and oxidation states of the material, which could explain the disproportion between the two techniques.

An interesting observation was made when we compared the SEM images of the high current density samples before and after catalysis. In Figure 21 we compare the high current density sample surface at pH 14 before (A) and after catalysis (B).

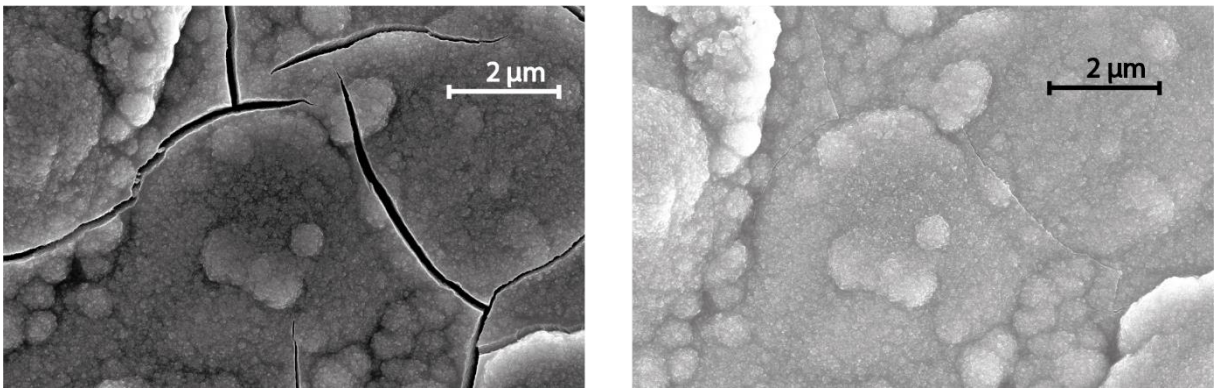

Figure 21. SEM image of the catalyst its surface before (A) and after catalysis (B) at a current density of -500 mA/cm² for 72h.

In this figure we see some major cracks actually fuse back together after catalysis. It appears that the increase in current density (and with that also the applied potential), actually has a sort of restorative effect on certain parts of catalyst surface, possibly due to re-deposition. Although this might suggest the surface roughness should have become smaller, this scale says very little of the nanometre scale surface effects. Channels/porosity can still form and cause high surface area, which are not observable at the micrometre scale.

Finally, we looked at the catalysis itself as a current density of -500 mA/cm² was applied on the catalysts for 72 h. In Figure 22 the three day transient chrono-potentiometry catalysis is displayed for both tested samples. In this figure we see the overpotential needed to maintain a current density of -500 mA/cm². The overpotential starts significantly higher than was needed to maintain a current density of -10 mA/cm², which is a logical consequence of increasing the current as stated by Ohmic's law (Formula 1).
In section 3.1 we suggested to increase the current density, to confirm if 6 M hydroxide was oversaturating the solution for a -10 mA/cm² current density. In that section it became apparent that the 6 M solution was not reducing the overpotential further for that given current density. Here the current density was increased severely and we see here that the higher current density does profit from a higher hydroxide concentration, as the overpotential is significantly lower than the 1 M hydroxide solution. This proves that for a current density of -10 mA/cm² a 1 M hydroxide solution is sufficient and only higher current densities require higher concentrations.
The alloy tested at pH 14.8 appears to lose stability over time as the overpotential increased by almost -0.3 V during the catalysis. This observation is explained by the still significant reduction of molybdenum from the alloy after catalysis, observed with EDX. The -500 mA/cm² current density at this pH does not appear sufficient to keep the overpotential stable for the catalytic alloy.
A positive point of notice here is that this experiment shows good promise for industry. In industry they often operate at even higher current densities and overpotentials [77], which could stabilize even the highest molarities of hydroxides. An important side note here is that this is only a result for the cathode and that the high current densities might have a negative effect on the anode. The anode already is a point of weakness, since oxidative processes tend to have a more destructive effect on the electrodes than reductive ones.

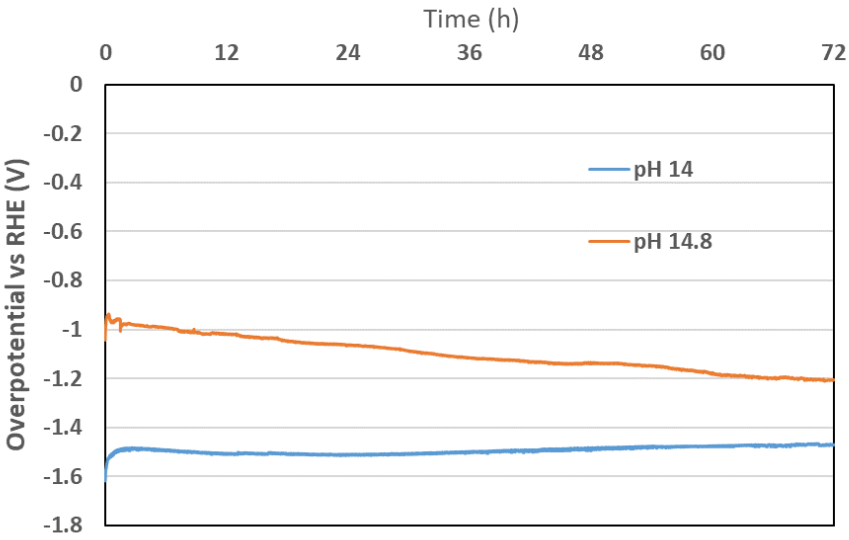

Figure 22. The transient chrono-potentiometry graph for 2 samples at a current density of -500 mA/cm². The overpotential changes over time were recorded to view the lowest overpotentials and efficiency over time.

3.2.4 Molybdate spiked electrolyte

Thermodynamics state that a chemical equilibrium is a function between reactants and products, and can be influenced by adding or subtracting any of those (Formula 3, section 1.2). The oxidation of molybdenum is, just like any chemical reaction, a product of an equilibrium between products and reactants. The oxidised state is strongly thermodynamically favourable, as was already seen in the last section.
In the following experiment the electrolyte solutions have been spiked with different molybdate to hydroxide ratios to see if this influences the roughness and final molybdate content at the catalyst surface. As stated before, molybdenum oxidises into the anionic molybdate via the reaction:

$$Mo + 8\,OH^- \rightleftharpoons MoO_4^{2-} + 4\,H_2O + 6\,e^-$$

By spiking the electrolyte solutions with the oxidation product molybdate, one could theoretically push the reaction back towards metallic molybdenum. In this experiment different ratios of molybdate-spiked electrolyte solutions were prepared and 3 day catalysis performed in it. As KOH causes the highest amount of loss in molybdenum from the alloy, this electrolyte solution has been spiked with molybdate. A ratio of 1:1, 1:3, 1:9 and 1:99 of MoO_4^{2-}:KOH respectively has been used. Here 0.5 M KOH was taken as the standard to keep electrolyte concentration around 1 M, and the ratio of molybdate was adjusted to this molarity. The loss in molybdenum content has been determined with EDX again and the RFI determined with the double layer capacitance. In Figure 23 we present the loss in molybdenum content for the different ratios of spiked molybdate.
There is a clear effect visible in Figure 23, as to how spiking the electrolyte solution with molybdate changes the total amount of molybdenum leached from the Ni-Mo alloy. The higher the ratio molybdate, the lower the loss in molybdenum is after catalysis. It is important here to note that EDX does not differentiate between molybdenum or molybdate. This means that there is no telling with this technique if we see a lower loss in molybdenum or possible residual molybdate from the electrolyte solution, that might have migrated into the alloy. However, by looking at the RFI we should be able to see if the alloy has roughened less for the higher spiked ratios.

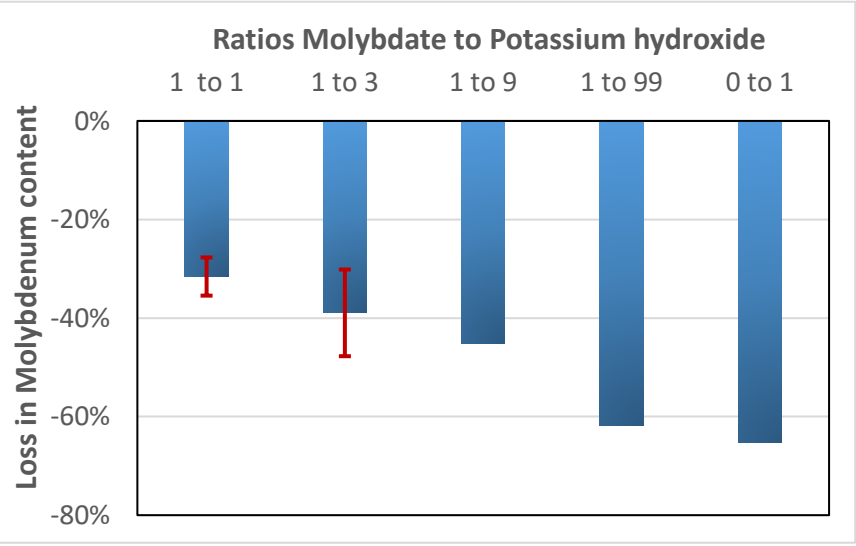

Figure 23. The effect of spiking the electrolyte solution with molybdate in different ratios, on the loss in molybdenum from the alloy after a catalysis time of 72h at a current density of -10 mA/cm². Measured with EDX

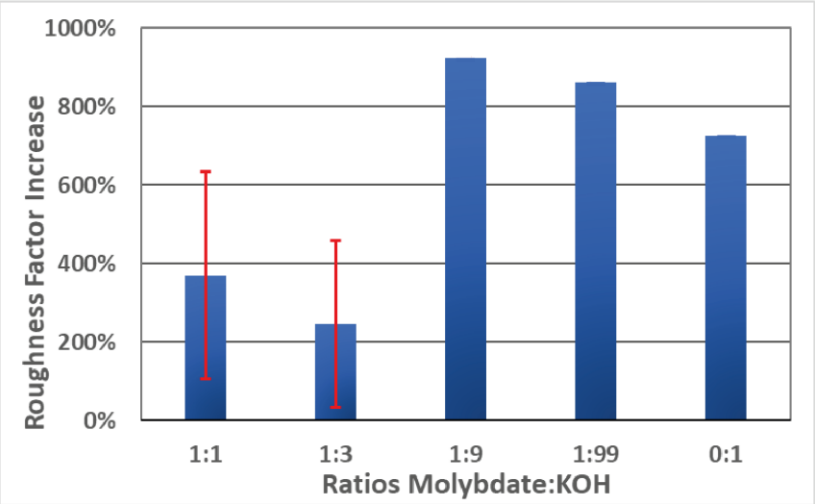

Figure 24. Roughness Factor Increases for the different ratios between molybdate and potassium hydroxide. Roughness factors calculated from CV measurements before and after 3 day catalysis at -10 mA/cm²

In Figure 24 the influence of the molybdate spiked electrolyte solutions on the RFI is presented. A strong reduction in RFI is visible for the 1:1 and 1:3 spiked electrolyte solutions, compared to the lower ratios. The effect on the RFI is stronger than what was observed for the loss in molybdenum, especially for the 1:3 ratio where we see the lowest increase in surface roughness. A direct correlation between the two techniques is less evident here than for earlier observations. In the 1:9 and 1:99 ratios an even higher surface roughness is observed, while with the EDX measurements we observe gradual increase in molybdenum loss when the molybdate ratio is reduced.

The results of these analysis techniques show how adding molybdate in high ratios to the electrolyte solution can actually shift the equilibrium back to metallic molybdenum, as a lower molybdenum loss and lower RFI is observed. Despite these results, the chrono-potentiometry reveal a side-effect of adding molybdate in high ratios to the electrolyte solution. When we look at Figure 25 we see the overpotential required to maintain the -10 mA/cm² current density. Here it becomes apparent that the addition of molybdate in high ratios has a negative effect on the potential required for hydrogen production. The overpotentials have become larger and shows erratic behaviour, especially for the 1:3 ratio.

The fact that the 1:3 ratio shows more erratic behaviour than the 1:1 ratio shows an interesting correlation between the overpotential and the RFI. The catalytic performance is connected to the increase in surface roughness and actually requires the increase to perform at the efficiency

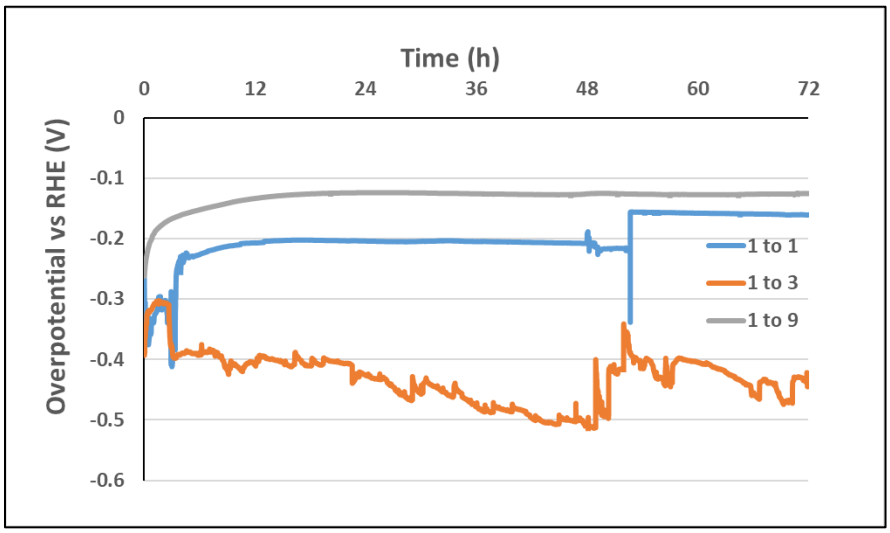

Figure 25. Transient chrono-potentiometry graph for the 1:1 (blue), 1:3 (orange) and 1:9 (grey) ratios molybdate to KOH.

The jump seen in the blue line around 50 h is an artefact caused by sudden motion of the cell during catalysis.

it does for Ni-Mo. At the 1:9 ratio, the performance is back to what is generally observed for the catalyst, which correlates back to the usually observed high increase in surface area during catalysis. Besides the lower RFI that might have influenced the catalytic performance, there is also the fact that a large amount of molybdate is present in the solution. The anionic molybdate itself is a larger molecule, which has a lower electrolytic mobility according to Stokes' law [78]. This can cause fluidic resistances to rise and with that increase the overpotential needed to maintain the applied current density.

Spiking the electrolyte solution with high molybdate ratios appears an effective way of reducing the amount of leaching through shifting of the chemical equilibrium. Both EDX and capacitance measurements display lower surface change. However, either the surface change is necessary to obtain low overpotentials or the molybdate interacts with the hydrogen production, since the catalytic activity goes down significantly for the higher ratios of molybdenum spiking. Finding an optimal ratio between hydroxide and molybdate might prove beneficial for stabilising the overpotential of the catalyst.
Nonetheless, spiking looks like an unfit candidate for industry as costs for the electrolyte solutions will rise significantly. This is not only due to the price of the molybdate, but also due to its molecular weight and relative high concentrations needed. For industrial scale electrolysers, kilograms of molybdate would need to be added to stabilise the Mo, losing its benefit of being a cheap electrocatalyst.

3.3 *In-situ* analysis

In-situ analysis is the act of observing changes in a system during a process, using different analysis techniques. The process that we aimed to analyse is the electro-catalysis, with a focus on the stability. Preparations were made to use *in-situ* liquid Atomic Force Microscopy (AFM) and *in-situ* UV-Vis spectrometry to analyse the processes around the electrolysis of water.
In-situ analysis offers a possibility to look at processes that would normally only be observed in snapshots, just like we performed with SEM-EDX and capacitance measurements (before and after catalysis). Furthermore, we are able to analyse the system out of equilibrium as is the case when we apply a potential difference.
For electrolysis of water, *in-situ* implies that the analysis techniques need to be performed in an electrochemical cell during the process of water splitting. Both for AFM and UV-Vis a new cell was designed which allowed analysis during electrolysis of water. In the following sections we will discuss how preparations were made for *in-situ* liquid AFM. Furthermore, some preliminary results are presented for (no current) liquid AFM to give an outlook to these promising techniques. The UV-Vis cell preparations and final design are presented in Appendix D.

3.3.1 In-situ liquid AFM analysis

The aim of using *in-situ* AFM is to see how the catalyst surface changes during catalysis. For *in-situ* AFM an electrochemical cell was designed and 3D printed, in which electrolysis of water could be performed while scanning the surface with an AFM tip. In Figure 26 we have presented the cell unloaded (Figure 26A) and loaded (Figure 26B) with a sample and electrolyte solution.
The cell consists of several components, such as a gas/liquid inlet and outlet (1a and 1b in Figure 26A) a platinum wire as counter electrode (2) a sample contact (3) and a solid, heavy metallic standard for AFM stability (4). Two copper wires are connected to the cell for connection to a potentiostat (5a + 5b). In Figure 26B we see how the cell looks when loaded with a sample and an electrolyte solution. The volume is around 5-10 mL and a sample of 1x1 cm is ideal for placement in the holder.

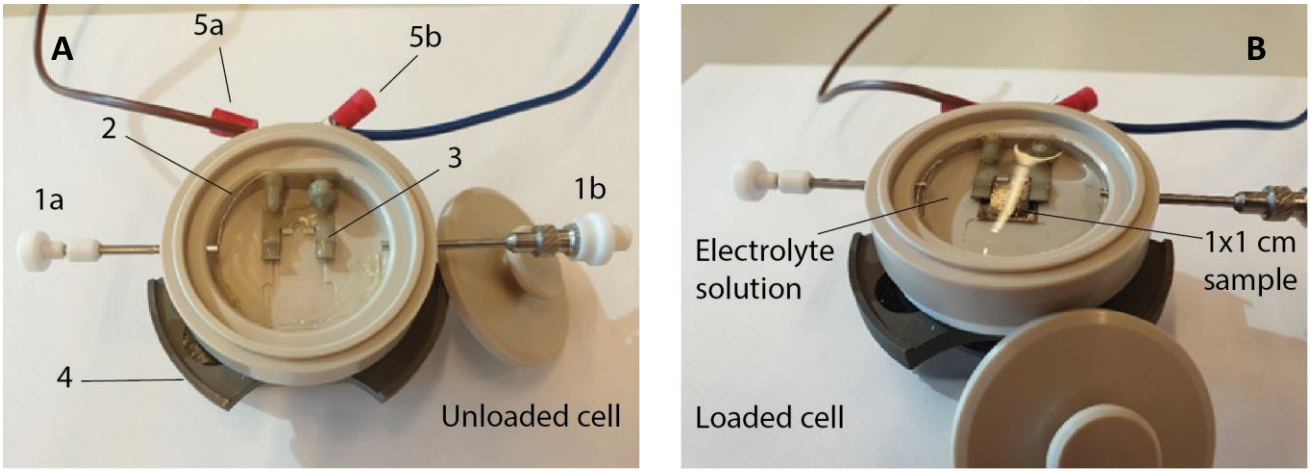

Figure 26. The 3D-printed electrochemical cell, specially designed for in-situ liquid AFM analysis.

The *in-situ* AFM measurement is an advanced technique and to prepare for it, liquid *in-situ* AFM was performed without a current in 1 M and 6 M KOH as described in the methodology. Since the cell in Figure 26 was specially designed for the *in-situ* experiment with current, it was not used for this experiment.
By selecting a silicon nitride tip (SiN_3) and using a fluid cell from Bruker, we could perform the experiment in a simpler set-up without current. In this fluid cell from Bruker a few drops of electrolyte solution are deposited on the sample, in which we performed the measurements. The tip then scanned until contact between sample and tip was lost or the electrolyte had evaporated. The composed height profile images, from the continuously scanned measurements, were used to construct roughness profiles. Four composed AFM images are shown in Figure 27 to give further elaboration to how the roughness profiles were created.

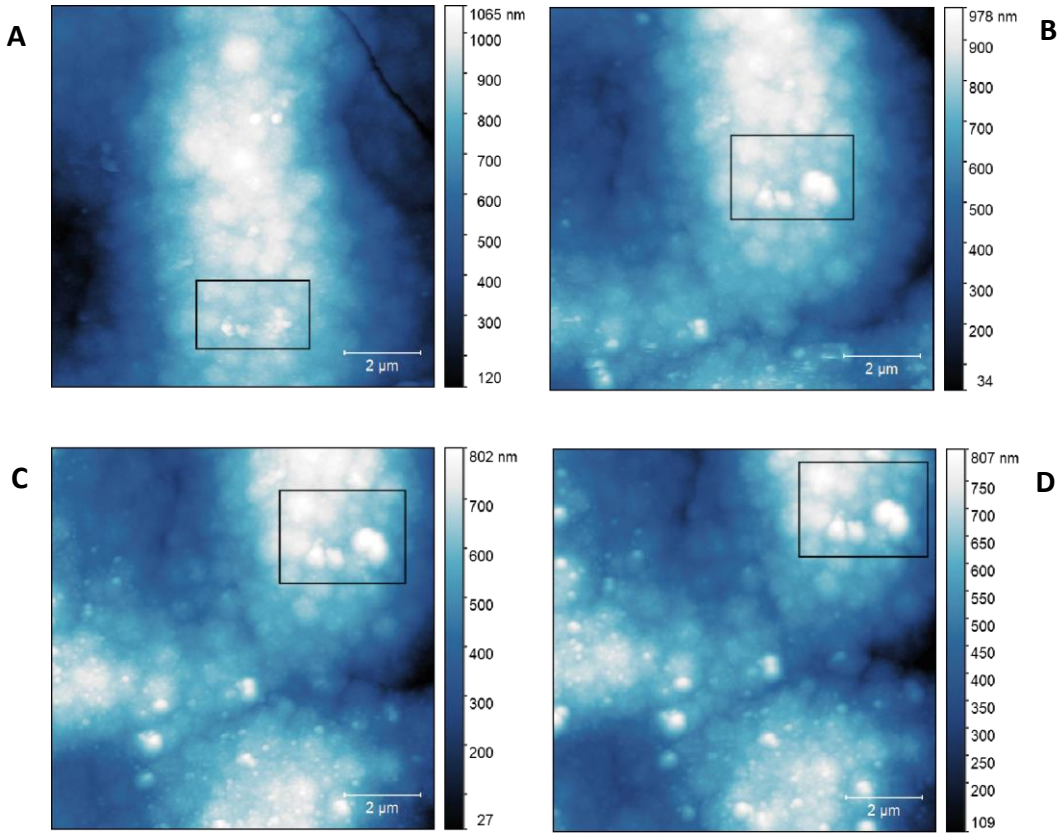

Figure 27. Four AFM images constructed after scanning the Ni-Mo alloys over a period of 6 hours in 6 M KOH with a SiN_3 probe. Drifting of samples causes the images to shift, selected windows show same spots, used for roughness calculation.

In Figure 27 we show the continuously probed area over 6 h for the 6 M KOH analysis. During scanning with the probe, the sample moved as can be seen in the masked areas. This is an effect known as drifting, due to the sample being submerged in a liquid. A realistic roughness determination was performed by masking a scanned location that could be observed in all images. The height changes for the masked areas were tracked over time and from those changes a roughness increase was calculated.
The same experiment was performed in water and in 1 M KOH, however the electrolyte solutions evaporated relatively quickly compared to the 6 M KOH concentration since high salinity decreases evaporation rates. AFM images from these samples are shown in Appendix E. Only the 6 M KOH concentration was stable long enough for leaching to occur significantly and to be visible with AFM. However, evaporation most likely occurred here as well, giving rise to the possibility of increasing pH as water evaporates and KOH remains.
Calculated roughness increases for the different electrolyte solutions are shown in Figure 28.

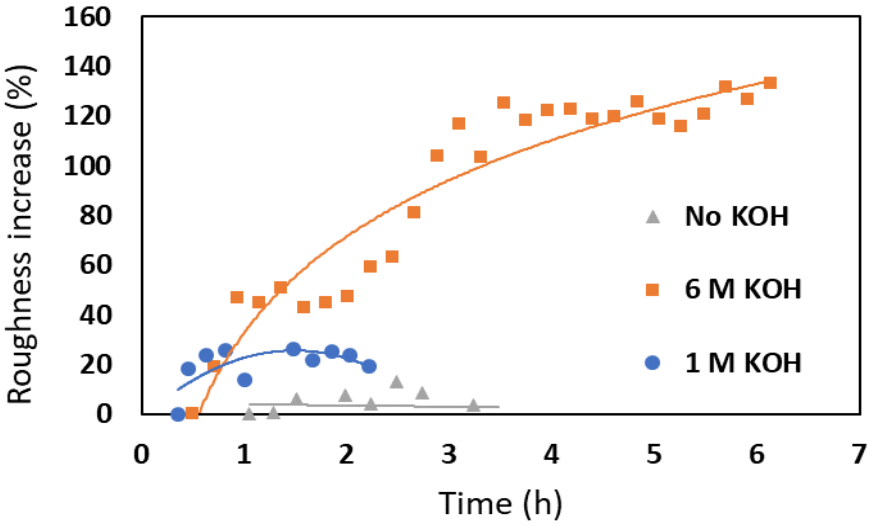

Figure 28. Roughness increases of Ni-Mo samples in different electrolyte solutions, measured with AFM. The starting point is thus 0%

In Figure 28 we see how only the sample in 6 M KOH shows a real roughness increase that could be tracked with AFM. In 1 M KOH the liquid evaporated too fast and the scan without KOH showed no change in roughness after about 3 hours. No useful time scales or data could be obtained for these two solutions.
There is quite some deviation from measured points (wavelike) to drawn curve for 6 M KOH. As the sample drifted (Figure 27), average roughness's could still be hard to determine. The roughness increase for 6 M KOH increased steadily for about 3-4 hours, after which it starts stabilising. This stabilisation time is in line with what we have seen for the activation time during catalysis. This observation further strengthens our argument that the activation time is caused by the increase in surface area due to the leaching of molybdenum from the alloy.
The fact that there is such a large difference between the capacitance roughness increase (RFI) (>600%) and the AFM roughness increase (<140%) has several explanations. First of all, AFM is not able to scan into the smallest pores, where capacity follows the surface down to the atomic level. As AFM only probes the surface, the porosity is neglected to a large extent. Secondly, the AFM samples could not be scanned for longer than 6 hours, which reduces further leaching as the liquid evaporated. Thirdly, as was discussed in the capacitance section, the RFI values measured with capacitance are likely higher than they actually are due to a loss in molybdenum content, which influences the alloy its specific capacitance. Also, current and potential effects are not taken into account. Finally, there is also the effect of using a different substrate (Ti foil vs Ti stub) of which the differences have not yet been analysed.
Despite the difference between AFM and capacitance, the most valuable information that we obtained with this technique is the time-profile for the surface change in 6 M KOH. The fact that we see the roughness increase, which subsequently stabilises, is perfectly in-line with what was seen for the activation times.

It would be of great interest to see the influence of the current on this roughening effect: would it increase more or less, faster or slower? Furthermore, by switching to our own designed AFM cell, the issue of liquid evaporating too fast could be prevented, as the volume is way larger (± 0.2 mL vs. ≥10 mL). This would make longer measurements possible. If the *in-situ* experiment while performing electrocatalysis with chrono-potentiometry succeeds, it could offer insight into current effects, leaching speed and correlate the surface area increase and activation time directly to each other.

3.4 Ni-Mo electrolytic selectivity

Since we observe Mo leaching, the electrochemical selectivity of the Ni-Mo electrocatalyst to produce hydrogen, was analysed by testing the Faradaic efficiency and by performing linear sweep voltammetry (LSV). By performing water splitting on the Ni-Mo catalyst in a H-cell which separates the OER from the HER, the volume of produced hydrogen could be compared with the applied current to calculate the Faradaic efficiency. To analyse if any other redox reactions were happening before and after catalysis, a linear sweep voltammogram was taken in the hydrogen production range.

3.4.1 Faradaic efficiency

The Faradaic efficiency was calculated using an advanced solar fuel set-up which has a gas-chromatograph (GC) connected to electrochemical instruments such as a potentiostat and an electrochemical cell. In the electrochemical cell, water splitting is performed in 1 M KOH at a current of 4 mA. The produced hydrogen is carried into the GC with a known krypton flow from which the amount can be calculated from the peak area. This produced hydrogen is then compared to the applied current, which indicates how much of the current went to hydrogen production.
A Faradaic efficiency of 100% means all the current is used for hydrogen production.
In Figure 29 we present the results for the Faradaic efficiency calculated from the GC.

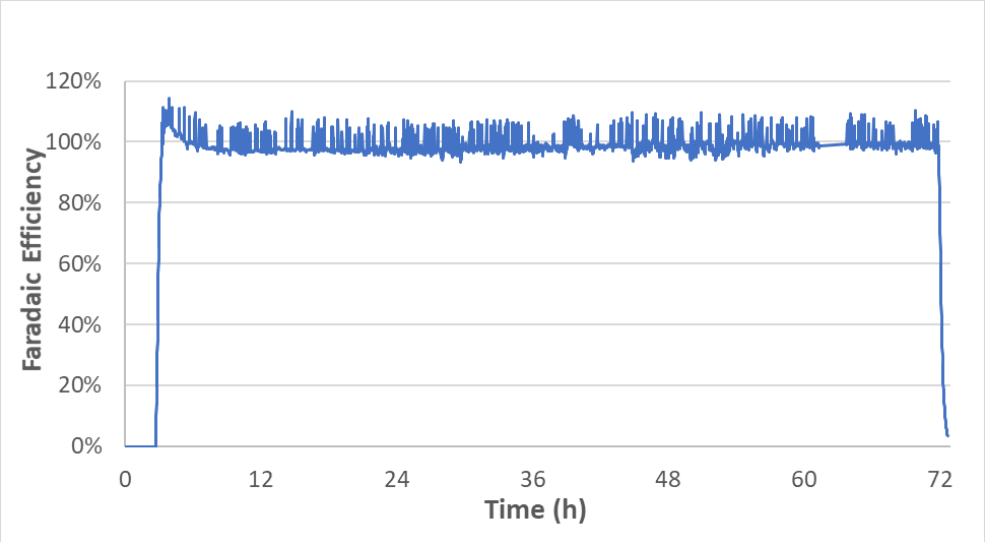

Figure 29. Faradaic efficiency of the HER on the Ni-Mo electrode during water splitting in 1 M KOH at a current of -4 mA

In Figure 29 we notice first off all that the line is highly erratic. This erratic behaviour occurs due to the separate flow injections, where after injection the detection reaches a short maximum peak before stabilising. This erratic behaviour can be considered background noise. The general trend in efficiency appears to lie around 100% for the largest part during electrolysis. However, in first 4-5 hours we observe an efficiency over 100% up to 115%. During this first 5 hours more hydrogen is produced then should be possible with the applied current. An average efficiency of the linear area was calculated and was found to be 98.63% ± 1.55%.

The first 5 hours is the time where molybdenum leaches out the strongest and the surface area becomes bigger, as was seen in the previous sections. This means that during the oxidation of molybdenum to molybdate, water is reduced non-Faradaically and molecular hydrogen is formed. This is to expected as the oxidation mechanism for molybdenum was only a half-reaction and will be assisted by a second half-reaction. If we take the HER in alkaline media as half-reaction we obtain a total reaction for the leaching of molybdenum:

Mo leaching half reaction:	Mo	+	$8\,OH^-$		→	MoO_4^{2-}	+	$4\,H_2O$	+	$6\,e^-$
HER:	$6\,H_2O$	+	$6\,e^-$		→	$6\,OH^-$	+	$3\,H_2$		
Total leaching reaction:	Mo	+	$2\,H_2O$	+ $2\,OH^-$	→	MoO_4^{2-}	+	$3\,H_2$		

The total reaction shows how during the electrolysis of water, molybdenum is oxidised to molybdate with as side-product extra hydrogen. Furthermore, the shape the curve takes in the first five hours looks like the inverse of the activation time that we have seen in section 3.1. It further proves that this activation time is an effect of the molybdenum leaching out and creating a larger surface area which activates the catalyst.

3.4.2 Linear Sweep Voltammetry

Linear sweep voltammetry is used to analyse the electrochemical selectivity towards the HER. By scanning over an overpotential range from 0 V to -0.6 V we are able to see if any side reactions are taking place at the electrode. This would be observable as extra current when scanning over the overpotential range.
Besides looking at side-reactions, a LSV scan is useful to see how strong a current appears over the overpotential range for each cation and hydroxide concentration. Although improving/analysing HER performance is not within the scope of this thesis, it does show what changing the electrolyte solution does to the efficiency of the catalysis. Due to the sheer number of catalyses that have been performed, only the LSV scan of KOH was chosen to be displayed here.

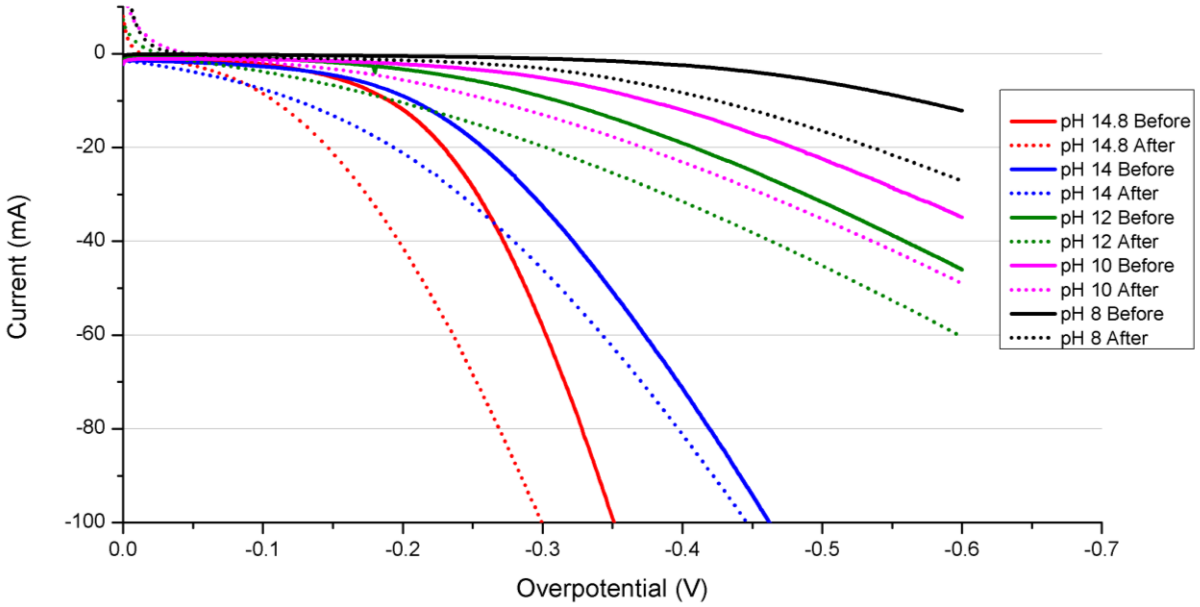

Figure 30. LSV scans before (solid) and after (dotted) catalysis for the KOH variations, scanned over a potential range of 0.6 V at the HER electrode.

In Figure 30 we show how the different variations of electrolyte solutions respond to overpotential. Notice how increasing the hydroxide concentration leads to higher currents obtained over the overpotential range. This is in line with what we have seen in Figure 22 where a higher current density was applied at a lower overpotential. Furthermore, it becomes apparent that every sample has become more efficient at the HER after 3 days of catalysis, obtaining higher currents at lower overpotentials. The increase in surface area observed in previous sections is likely the cause for this effect.
During all LSV scans no side reactions occurred that showed additional current appear over the scanning range. Together with the Faradaic efficiency results, the reaction appears to have a near 100% selectivity towards the HER. As we are working with chemicals of trace metal quality, side reactions due to impurities are minimal thus obtaining such high selectivity.

4. Summary

The Ni-Mo electrocatalyst its high efficiency in alkaline water splitting was discussed in literature [56] to be due to one of three mechanisms. The three mechanisms being: the Sabatier principle, the spill-over effect and an increase in surface area. In previous research [57], [73] it was found that molybdenum leaches out the surface of the catalyst and that cations influenced the rate and strength of this leaching. This research focussed on how the electrolyte solution influenced this leaching and how the leaching effects the catalytic process.

We observed during all catalyses that there was an activation time for the catalyst to reach its peak efficiency as was summarised in Table 2. By analysing the surface of the catalyst with SEM-EDX and capacitance measurements, it became apparent that the surface area became larger due to a loss in molybdenum content. Here the cation potassium lead to highest increase in surface area and leaching of molybdenum, most likely due to its higher solubility. Furthermore, we saw that the oxidation of molybdenum was heavily stimulated by an increase in hydroxide concentration, with a concentration of 6 M leaching the strongest. This is expected since hydroxides are part of the oxidation half reaction of molybdenum. However, this might also explain why oxidation occurs at a reductive potential, since a higher hydroxide concentration pushes the reaction equilibrium towards its products (molybdate).

By spiking the electrolyte solution with molybdate, we were able to reduce surface roughening to a large extend. However, this led to large overpotentials indicating that surface roughening is an important facet for Ni-Mo obtaining its high performance. A side note for this experiment was that the influence of the high concentration of molybdate might also have increased the overpotential, due to being a larger anion increasing the fluid resistance.
When we looked at a pure nickel electrode, there is deactivation of the catalyst due to the formation of hydrides (Figure 12). Molybdenum plays a crucial role in preventing this, since this is not observed for a Ni-Mo electrode. This means its effectivity is not solely explained by a high surface area, but that there is a synergy or spill-over effect present as well. This differs from Raney nickel, as the goal there is to remove as much as the secondary metal to obtain an as high as possible surface area.
Furthermore, liquid AFM linked the increase in surface area to the activation time that was observed during catalysis. The liquid AFM measurement was performed without current, but showed that roughness increases fast at the start in alkaline solutions and flattens/stabilises after a while. *In-situ* AFM should link the activation time and roughness increase with higher certainty as current and potential influences can then be taken into account.

ICP-AES showed how there is almost no leaching of molybdenum below pH 12. This indicates us that the high hydroxide concentration is the reason molybdenum is able to oxidise at a reductive potential. However, nickel loses its stability below a pH of 12 as nickel is protected by a thin oxide layer which is lost at lower pH [76].
The leaching of molybdenum was then attempted to be controlled by increasing the current density from -10 mA/cm^2 to -500 mA/cm^2. Here we found that increasing the reductive potential around the electrode was able to lower the loss in molybdenum significantly. With

SEM-EDX we even observed a "self-healing" effect on the alloy, healing cracks that were there before catalysis. This is most likely due to re-deposition, although this was not further researched. The catalytic alloy appears to becomes more stable, the higher the reductive potential applied on the electrode.
When we analysed the faradaic efficiency we observed a close to 100% efficiency with the GC. During the first hours we noticed extra hydrogen being produced, obtaining efficiencies up to 115%. As this overproduction had the inverse shape of the activation effect, this observation could be ascribed to the oxidation of molybdenum. Using this data, a total reaction of molybdenum to molybdate could be determined, where 3 extra hydrogen molecules were formed for each molybdenum atom oxidised.

5. Conclusions

In this thesis, the electrolyte effects on the stability of the Ni-Mo electrocatalyst was researched in depth. By variating the cations and hydroxide concentrations in the electrolyte solution during alkaline water splitting, their influences on the catalyst its surface structure were studied.

We found that the hydroxide concentration is the main incentive that pushes the equilibrium towards molybdate, overcoming the reductive potential around the electrode. Furthermore, we noticed with EDX and capacitance measurements that when using potassium as cation the amount of molybdenum that leached from the electrode doubled, most likely due to a solubility effect.

The activation time seen for the catalyst is caused by the increase in surface area due to leaching of molybdenum as was seen with liquid AFM. Further proof was obtained when the Faradaic efficiency was calculated, where an efficiency of 115% was obtained in the first hours. This efficiency of 115% was explained to be due to extra hydrogen production from the molybdenum oxidation.

The high surface area due to the leaching of molybdenum appears to be the most important mechanism for the Ni-Mo its high efficiency as an electrocatalyst. However, molybdenum is certainly necessary in amounts to circumvent the formation of nickel hydrides and prevent deactivation.

Finally, we found that increasing the current density to -500 mA/cm^2 lowered the loss in molybdenum significantly from 71% to only 18% after catalysis and we observed a restorative effect on the alloy with SEM, restoring cracks that were there before catalysis.

6. Outlook

In order to build further on this project, several recommendations can be made to deeper the understanding around the processes of the Ni-Mo electrocatalyst.

To complete the picture around molybdenum leaching the *in-situ* UV-Vis measurements during alkaline water splitting would be of great value. With this technique we could determine a rate at which molybdenum is oxidised to molybdate.

We have seen with liquid AFM in 6 M KOH how the surface roughness increases over the 6 h that could be measured. By performing *in-situ* AFM one could further determine the effects of the current and potential on the increase in surface area. The liquid AFM we performed only looked at the surface without current, potential differences or bubble formation, which gives an incomplete picture of the actual situation during catalysis. Furthermore, with the liquid AFM used in this research, the electrolyte solution evaporated too fast which made low solutes studying impossible. Our own designed *in-situ* AFM cell has far more volume, which should circumvent this issue.

The reproducibility of the alloy thickness could be improved by further looking into electrodeposition parameters. It was noticed during deposition that the solution turned darker after several depositions. Renewing deposition baths more quickly, or adjusting the time at which current is applied to obtain equally thick coatings are possible solutions to this.

One technique that has not been used in this research, but could give valuable information, is ellipsometry. This technique was not available at our department but has been of interest since the start of this research. Ellipsometry could offer new insights into roughness, composition, coating thickness and more.

The 'self-healing' effect that was observed for higher current densities could be further explored for even higher current densities and for larger (industrial) electrodes. The observed effect is a promising outlook for upscaling and actual testing on industrial scale. If higher current densities up to 1 A/cm^2 could resist the higher hydroxide concentrations (6 M or even higher) it could prove to be an already viable option for industry. Equipment for 1 A/cm^2 of higher is not available at our department at the moment, but with a simple potentiostat upgrade some interesting new paths could open up.

7. Acknowledgements

As a student that first did an applied bachelor (Dutch: HBO) I first made my entrance in a Debye research group during my master thesis. I knew I wanted to do something with renewable energy and that is why I contacted Jochem Wijten for a project. Jochem sparked my interest with the production of molecular hydrogen and electrochemistry. During my thesis he learned me all the theoretical aspects and analysis techniques that come with advanced electro-analysis. I enjoyed the way we could have both informal (on the lab, during drinks) and formal talks (practising presentations, explanations, feedback). He always gave space for my own development and my own project, where I decided the boundaries and where I could always ask for assistance where I needed it. For me personally, we had the ideal student/supervisor relationship. Thank you for this experience Jochem, I hope you enjoyed it as much as I did.
Secondly, I would like to thanks Tess van Eeden, Jochem's bachelor student when I started my master thesis. Tess offered me great support on the lab, helping me to get around in this new environment. Having a sitting place next to each other gave me a head start in understanding the basics at both electrochemistry and how things worked at ICC.
Then I would like to thank my first and second examiners, Prof. Dr. Ir. Bert Weckhuysen and Dr. Florian Meirer. Thank you for giving me the opportunity to do my Master thesis at the Inorganic Chemistry & Catalysis group.

Furthermore, I would to thank all the people that assisted me during my research. Laurens Mandemaker for doing the liquid AFM measurements, Dennie Wezendonk for introduction into XRD (although the data was regrettably not of use due to our samples being amorphous), Oscar Kerkenaar for technical assistance, Coen Mulder from TNO for doing ICP-AES measurements and of course my fellow students for the helpful discussions and reflecting on discovered results. Special thanks to Thimo Jacobs, Jim de Ruiter and our pre-master group, Arend, Allesio, Hedera and Georgia for making this time towards my thesis so pleasant.

Finally, I would like to thank my partner Willeke coping with me for the last few weeks leading up to finishing this thesis. Thank you for being patient with me, listening to me, helping me with wherever needed and preparing our 6-month adventure to Copenhagen for my final internship. I could not have done this without you.

References

[1] World Bank, International Energy Agency, "Access to electricity (% of population)," *Sustainable Energy for All (SE4ALL) database from the SE4ALL Global Tracking Framework*, 2018. [Online]. Available: https://data.worldbank.org/indicator/EG.ELC.ACCS.ZS. [Accessed: 10-Jan-2019].

[2] Enerdata, "Global Energy Trends, 2018 edition. A step backward for the energy transition?," *30 may*, 2018. [Online]. Available: https://www.enerdata.net/publications/reports-presentations/2018-world-energy-trends-projections.html. [Accessed: 29-Jan-2019].

[3] IEA, "Renewables 2017," *IEA Publications*, 2017. [Online]. Available: https://www.iea.org/media/publications/mtrmr/Renewables2017ExecutiveSummary.PDF. [Accessed: 29-Jan-2019].

[4] N. Scarlat, J. F. Dallemand, F. Monforti-Ferrario, M. Banja, and V. Motola, "Renewable energy policy framework and bioenergy contribution in the European Union - An overview from National Renewable Energy Action Plans and Progress Reports," *Renew. Sustain. Energy Rev.*, vol. 51, pp. 969–985, 2015.

[5] S. Solomon, G. Plattner, R. Knutti, and P. Friedlingstein, "Irreversible climate change due to carbon dioxide emissions," *Proc. Natl. Acad. Sci.*, vol. 106, no. 6, pp. 1704–1709, 2009.

[6] D. O. Rourke and S. Connolly, "Just Oil? The Distribution of Environmental And Social Impacts of Oil Production and Consumption," *Annu. Rev. Environ. Resour.*, vol. 28, no. 1, pp. 587–617, 2003.

[7] J. . Sarmiento and U. Siengenthaler, "Atmospheric carbon dioxide and the ocean," *Nature*, vol. 365, pp. 119–125, 1993.

[8] N. Armaroli and V. Balzani, "Solar Electricity and Solar Fuels : Status and Perspectives in the Context of the Energy Transition," *Chem. Eur. J.*, vol. 22, pp. 32–57, 2016.

[9] Nathan S. Lewis, "Research opportunities to advance solar energy utilization," *Science (80-.).*, vol. 351, no. 6271, pp. 353–363, 2016.

[10] K. Bhowmick and M. Narvekar, "Trajectory outlier detection for traffic events: A survey," *Adv. Intell. Syst. Comput.*, vol. 673, pp. 37–46, 2018.

[11] H. Ibrahim, A. Ilinca, and J. Perron, "Energy storage systems — Characteristics and comparisons,", *Renewable and Sustainable Energy reviews,* vol. 12, pp. 1221–1250, 2008.

[12] N. K. C. Nair and N. Garimella, "Battery energy storage systems: Assessment for small-scale renewable energy integration," *Energy Build.*, vol. 42, no. 11, pp. 2124–2130, 2010.

[13] C. Abbey and G. Joos, "Supercapacitor Energy Storage for Wind Energy Applications," *IEEE Trans. Ind. Appl.*, vol. 43, no. 3, pp. 769–776, 2007.

[14] H. Liu and J. Jiang, "Flywheel energy storage — An upswing technology for energy sustainability,", *Energy & Buildings,* vol. 39, pp. 599–604, 2007.

[15] S. Rehman, L. M. Al-Hadhrami, and M. M. Alam, "Pumped hydro energy storage system: A technological review," *Renew. Sustain. Energy Rev.*, vol. 44, pp. 586–598, 2015.

[16] M. Jefferson, "A renewable energy future?," *Handb. Energy Clim. Chang.*, vol. 285, no. x, pp. 687–690, 2013.

[17] G. W. Crabtree, M. S. Dresselhaus, and M. V Buchanan, "The Hydrogen Economy," *Phys. Today*, vol. 1, pp. 39–45, 2004.

[18] J. O. M. Bockris, "The hydrogen economy : Its history," *Int. J. Hydrogen Energy*, vol. 38, no. 6, pp. 2579–2588, 2012.

[19] J. Verne, "The Mysterious Island," in *The Mysterious Island*, Hetzel, 1874, p. 229.

[20] K. Zeng and D. Zhang, "Recent progress in alkaline water electrolysis for hydrogen production and applications," *Prog. Energy Combust. Sci.*, vol. 36, no. 3, pp. 307–326, 2010.

[21] J. Divisek, H. Schmitz, and B. Steffen, "Electrocatalyst Materials for Hydrogen Evolution," *Electrochem. Acta*, vol. 39, no. 11, pp. 1723–1731, 1994.

[22] L. Zhou, "Progress and problems in hydrogen storage methods," *Renew. Sustain. Energy Rev.*, vol. 9, pp. 395–408, 2005.

[23] A. Züttel, "Materials for hydrogen storage," *Mater. Today*, vol. 6, no. 9, pp. 24–33, 2003.

[24] B. Sakintuna, F. Lamari-darkrim, and M. Hirscher, "Metal hydride materials for solid hydrogen storage : A review," *Int. J. Hydrogen Energy*, vol. 32, pp. 1121–1140, 2007.

[25] N. L. Rosi *et al.*, "Hydrogen Storage in Microporous Metal-Organic Frameworks," *Science (80).*, vol. 300, no. 5622, pp. 1127–1129, May 2003.

[26] W. Wang, S. Wang, X. Ma, J. Gong, and W. Wang, "Recent advances in catalytic hydrogenation of carbon dioxide," *Chem. Soc. Rev.*, vol. 40, no. 7, pp. 3703–3727, 2011.

[27] X.-M. Liu, G. Q. Lu, Z.-F. Yan, and J. Beltramini, "Recent Advances in Catalysts for Methanol Synthesis via Hydrogenation of CO and CO2," *Ind. Eng. Chem. Res.*, vol. 42, no. 25, pp. 6518–6530, Dec. 2003.

[28] G. Centi and S. Perathoner, "Opportunities and prospects in the chemical recycling of carbon dioxide to fuels," *Catal. Today*, vol. 148, no. 3, pp. 191–205, 2009.

[29] J. Thangavelautham, D. Dewitt, and S. Dubowsky, "The design of long-life , high-efficiency PEM fuel cell power supplies for low power sensor networks," *Int. J. Hydrogen Energy*, vol. 42, no. 31, pp. 20277–20296, 2017.

[30] Y. Yamada *et al.*, "One chip photovoltaic water electrolysis device," *Int. J. Hydrogen Energy*, vol. 28, no. 11, pp. 1167–1169, 2003.

[31] R. W. Revie and H. H. Uhlig, "Effect of stress: Fretting Corrosion," in *CORROSION AND CORROSION CONTROL An Introduction to Corrosion Science and Engineering*, 2008, pp. 180–184.

[32] M. Favaro *et al.*, "direct probing of the solid / liquid interface," *Nat. Commun.*, vol. 7, no. 12695, pp. 1–8, 2016.

[33] A. Lavacchi, "A Bird's Eye View of Energy-Related Electrochemistry," in *Nanotechnology in Electrocatalysis for Energy*, New York: Springer Science+Business Media, 2013, pp. 25–61.

[34] Z. W. She, J. Kibsgaard, C. F. Dickens, I. Chorkendorff, J. K. Nørskov, and T. F. Jaramillo, "Combining theory and experiment in electrocatalysis: Insights into materials design," *Science (80-.).*, vol. 355, no. 6321, 2017.

[35] N. Mahmood, Y. Yao, J. W. Zhang, L. Pan, X. Zhang, and J. J. Zou, "Electrocatalysts for Hydrogen Evolution in Alkaline Electrolytes: Mechanisms, Challenges, and Prospective Solutions," *Adv. Sci.*, vol. 5, no. 2, 2018.

[36] M. Gali, A. Lewandowski, and I. St, "Ionic liquids as electrolytes," *Electrochminica Acta*, vol. 51, pp. 5567–5580, 2006.

[37] N. Sato, *Electrochemistry at metal and semiconductor electrodes*, 1st ed. Amstedam: Elsevier, 1998.

[38] N. Eliaz and E. Gileadi, *Physical Electrochemistry: Fundamentals, Techniques, and Applications*. Wiley-Vch, 2018.

[39] D. Lackey, J. Schott, and B. Straehler, "Electrochemical double layer simulations by halogen , alkali and hydrogen coadsorption with water on metal surfaces," *Surf. Sci.*, vol. 247, pp. 239–247, 1991.

[40] D. C. Grahame, "The Eelectrical Double Layer and the Theory of Electrocapillarity," *Chem. Rev.*, vol. 41, no. 3, pp. 441–501, 1947.

[41] N. V. Krstajić, V. D. Jović, L. Gajić-Krstajić, B. M. Jović, A. L. Antozzi, and G. N. Martelli, "Electrodeposition of Ni-Mo alloy coatings and their characterization as cathodes for hydrogen evolution in sodium hydroxide solution," *Int. J. Hydrogen Energy*, vol. 33, no. 14, pp. 3676–3687, 2008.

[42] X. Li, P. F. Liu, L. Zhang, M. Y. Zu, Y. X. Yang, and H. G. Yang, "Enhancing alkaline hydrogen evolution reaction activity through Ni–Mn $_3$ O $_4$ nanocomposites," *Chem. Commun.*, vol. 52, no. 69, pp. 10566–10569, 2016.

[43] M. E. Tuckerman, D. Marx, and M. Parrinello, "The nature and transport mechanism of hydrated hydroxide ions in aqueous solution," *Nature*, vol. 417, pp. 925–929, 2002.

[44] M. Gong, D. Y. Wang, C. C. Chen, B. J. Hwang, and H. Dai, "A mini review on nickel-based electrocatalysts for alkaline hydrogen evolution reaction," *Nano Res.*, vol. 9, no. 1, pp. 28–46, 2016.

[45] F. Safizadeh, E. Ghali, and G. Houlachi, "Electrocatalysis developments for hydrogen evolution reaction in alkaline solutions - A Review," *Int. J. Hydrogen Energy*, vol. 40, no. 1, pp. 256–274, 2015.

[46] J. Divisek, H. Schmitz, and J. Balej, "Ni and Mo coatings as hydrogen cathodes," *J. Appl. Electrochem.*, vol. 19, no. 4, pp. 519–530, 1989.

[47] D. E. Brown, M. N. Mahmood, M. C. M. Man, and A. K. Turner, "Preparation and characterization of low overvoltage transition metal alloy electrocatalysts for hydrogen evolution in alkaline solutions," *Electrochim. Acta*, vol. 29, no. 11, pp. 1551–1556, 1984.

[48] A. B. Laursen *et al.*, "Electrochemical hydrogen evolution: Sabatiers principle and the volcano plot," *J. Chem. Educ.*, vol. 89, no. 12, pp. 1595–1599, 2012.

[49] A. R. Zeradjanin, J. P. Grote, G. Polymeros, and K. J. J. Mayrhofer, "A Critical Review on Hydrogen Evolution Electrocatalysis: Re-exploring the Volcano-relationship," *Electroanalysis*, vol. 28, no. 10, pp. 2256–2269, 2016.

[50] M. Carmo, D. L. Fritz, J. Mergel, and D. Stolten, "A comprehensive review on PEM water electrolysis," *Int. J. Hydrogen Energy*, vol. 38, no. 12, pp. 4901–4934, 2013.

[51] J. Zheng, W. Sheng, Z. Zhuang, B. Xu, and Y. Yan, "Universal dependence of hydrogen oxidation and evolution reaction activity of platinum-group metals on pH and hydrogen binding energy," *Sci. Adv.*, vol. 2, no. 3, pp. 1–8, 2016.

[52] K. Hu, S. Jeong, M. Wakisaka, J. Fujita, and Y. Ito, "Bottom-up Synthesis of Porous NiMo Alloy for Hydrogen Evolution Reaction," *Metals (Basel).*, vol. 8, no. 2, p. 83, 2018.

[53] C. C. L. McCrory, S. Jung, I. M. Ferrer, S. M. Chatman, J. C. Peters, and T. F. Jaramillo, "Benchmarking Hydrogen Evolving Reaction and Oxygen Evolving Reaction Electrocatalysts for Solar Water Splitting Devices," *J. Am. Chem. Soc.*, vol. 137, no. 13, pp. 4347–4357, 2015.

[54] J. H. J. Wijten, R. P. H. Jong, G. Mul, and B. M. Weckhuysen, "Cathodic Electro-deposition of Ni-Mo on Semiconducting NiFe2O4 for Photo-electrochemical Hydrogen Evolution," *ChemSusChem*, vol. 11, no. 8, pp. 1374–1381, 2018.

[55] J. Zhang *et al.*, "Efficient hydrogen production on MoNi4 electrocatalysts with fast water dissociation kinetics," *Nat. Commun.*, vol. 8, no. May, pp. 1–8, 2017.

[56] J. R. McKone, S. C. Marinescu, B. S. Brunschwig, J. R. Winkler, and H. B. Gray, "Earth-abundant hydrogen evolution electrocatalysts," *Chem. Sci.*, vol. 5, no. 3, pp. 865–878, 2014.

[57] R. L. Riemersma, J. Wijten, "Stability of Ni-Mo Electrocatalysts Employed in Water Splitting," Master Thesis, University Utrecht, 2018.

[58] M. Schalenbach *et al.*, "Nickel-molybdenum alloy catalysts for the hydrogen evolution reaction: Activity and stability revised," *Electrochim. Acta*, vol. 259, pp. 1154–1161, 2017.

[59] M. N. Hull, "On The Anodic Dissolution Of Molybdenum In Acidic And Alkaline Electrolytes," *Interfacial Electrochem.*, vol. 38, no. Vi, 1972.

[60] M. deKay Thompson and A. L. Kaye, "The electrochemical oxidation of molybdenum in potassium hydroxide solutions," *Trans. Electrochem. Soc.*, vol. 62, no. 1, pp. 255–265, 1932.

[61] G. S. Tasic, S. P. Maslovara, D. L. Zugic, A. D. Maksic, and M. P. Marceta Kaninski, "Characterization of the Ni-Mo catalyst formed in situ during hydrogen generation from alkaline water electrolysis," *Int. J. Hydrogen Energy*, vol. 36, no. 18, pp. 11588–11595, 2011.

[62] C. T. Bowen, H. J. Davis, B. F. Henshaw, R. Lachance, R. L. LeRoy, and R. Renaud, "Developments in advanced alkaline water electrolysis," *Int. J. Hydrogen Energy*, vol. 9, no. 1–2, pp. 59–66, Jan. 1984.

[63] M. Gong *et al.*, "Nanoscale nickel oxide/nickel heterostructures for active hydrogen evolution electrocatalysis," *Nat. Commun.*, vol. 5, pp. 1–6, 2014.

[64] M. Manazoğlu, G. Hapçı, and G. Orhan, "Effect of electrolysis parameters of Ni–Mo alloy on the electrocatalytic activity for hydrogen evaluation and their stability in alkali medium," *J. Appl. Electrochem.*, vol. 46, no. 2, pp. 191–204, 2016.

[65] S. Trasatti, "Work function, electronegativity, and electrochemical behaviour of metals. III. Electrolytic hydrogen evolution in acid solutions," *J. Electroanal. Chem.*, vol. 39, no. 1, pp. 163–184, 1972.

[66] S. S. Djokiç, "Electrodeposition and Charaterization of Alloys and Composite Materials," in *Electrodeposition and Surface Finishing*, 57th ed., R. E. White, Ed. New York: Springer, 2014, pp. 1–23.

[67] E. J. Sun, S., & Podlaha, "Electrodeposition of Mo-rich, MoNi alloys from an aqueous electrolyte," *J. Electrochem. Soc.*, vol. 159, no. 2, pp. D97–D102, 2011.

[68] D. Podlaha, E. J., & Landolt, "Induced codeposition III. Molybdenum alloys with nickel, cobalt, and iron.," *J. Electrochem. Soc.*, vol. 144, no. 5, pp. 1672–1680, 1997.

[69] D. Podlaha, E. J., & Landolt, "Induced Codeposition II. A Mathematical Model Describing the Electrodeposition of Ni-Mo Alloys," *J. Electrochem. Soc.*, vol. 143, no. 3, pp. 893–899, 1996.

[70] P. T. Kissinger and W. R. Heineman, "Cyclic voltammetry," *J. Chem. Educ.*, vol. 60, no. 9, p. 702, 1983.

[71] G. A. Mabbott, "An Introduction to Cyclic Voltammetry," *J. Chem. Educ.*, vol. 60, no. 9, pp. 697–702, 1983.

[72] G. Binnig, C. F. Quate, and C. Gerber, "Atomic Force Microscope," *Phys. Rev. Lett.*, vol. 56, no. 9, pp. 930–933, Mar. 1986.

[73] J. H. J. Wijten *et al.*, "Electrolyte Effects on the Stability of Ni-Mo Cathodes for the Hydrogen Evolution Reaction," *(under Constr.*, 2019).

[74] D. M. Soares, O. Teschke, and I. Torriani, "Hydride Effect on the Kinetics of the Hydrogen Evolution Reaction on Nickel Cathodes in Alkaline Media," *J. Electrochem. Soc.*, vol. 139, no. 1, p. 98, 1992.

[75] R. K. Shervedani and A. Lasia, "Study of the hydrogen evolution reaction on Ni-Mo-P electrodes in alkaline solutions," *J. Electrochem. Soc.*, vol. 145, no. 7, p. 2219, 1998.

[76] R. J. J. Smith and E. D. Verink, "The Passivation of Nickel in Aquous Solutions--I. The Identification of Insoluable Corrosion Pruducts on Nickel Electrodes Using Optical and ESCA Techniques," *Corros. Sci.*, vol. 27, no. 8, pp. 803–813, 1987.

[77] R. L. Leroy, "Industrial Water Electrolysis: Present And Future," *Int. J. Hydrog. Energy*, vol. 8, no. 6, pp. 401–417, 1983.

[78] L. Onsager, "Report on a revision of the conductivity theory," *Trans. Faraday Soc.*, vol. 23, pp. 341–349, 1927.

[79] M.P. Pavlov, N.V. Morozova, V.N. Kudryavtsev, "Electrodeposition of nickel-molybdenum alloys from ammonium citrate baths containing intermediate valence molybdenum compounds," *Protection of Metals,* Vol. 43, Issue 5, pp 459–464, 2007.

Appendices

Appendix A – activation times

In this appendix the different transient chrono-potentiometry for all the pH and cation variations are presented. The goal of this appendix is to show that all samples showed an activation time before reaching their lowest overpotential. Only the first chrono-potentiometry of each of the duplo experiments is presented here to avoid confusion.

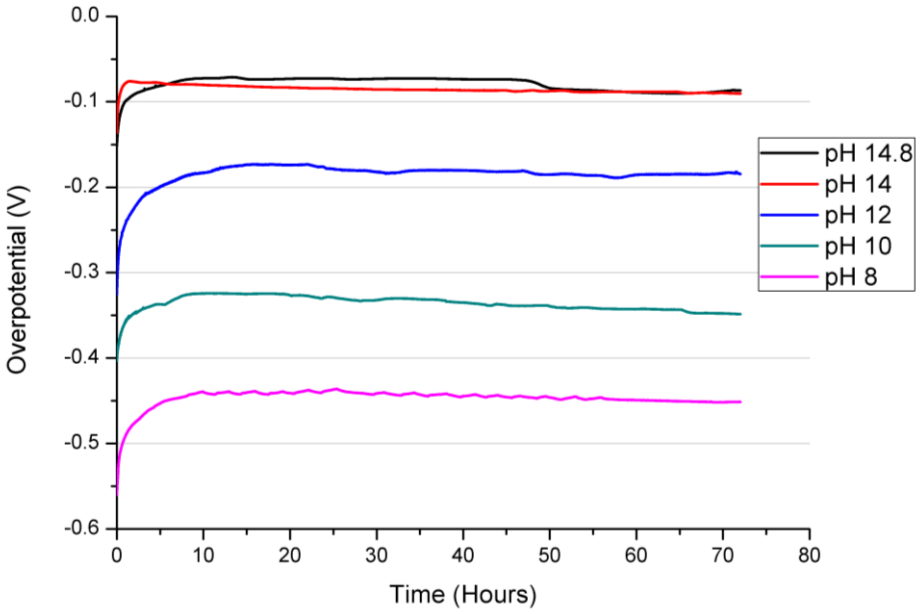

Appendix Fig. 1. Transient chrono-potentiometry for the sodium (Na) pH series. Activation times were visible for each in the series

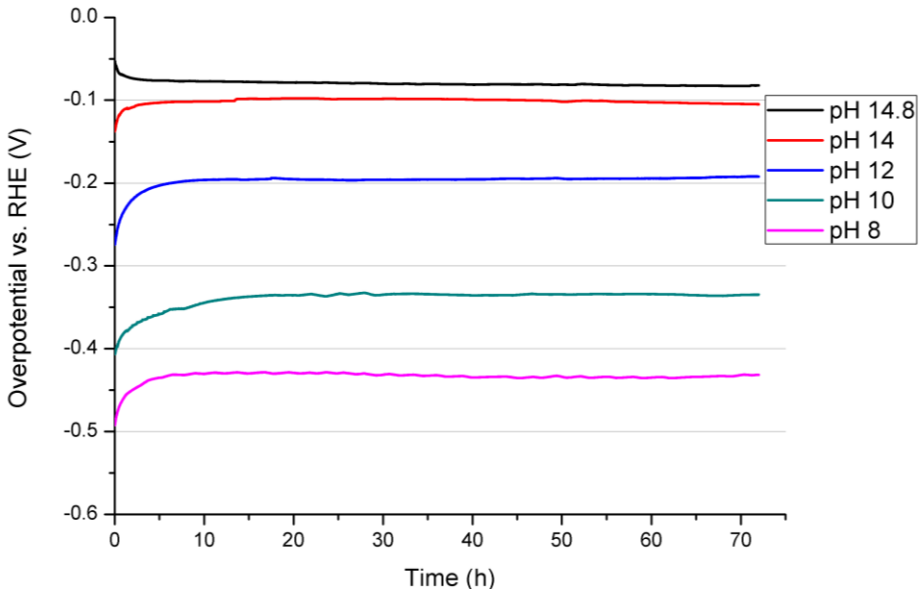

Appendix Fig. 2. Transient chrono-potentiometry for the potassium (K) pH series. Activation times were visible for each in the series except 14.8, which started lower than normal (instant activation)

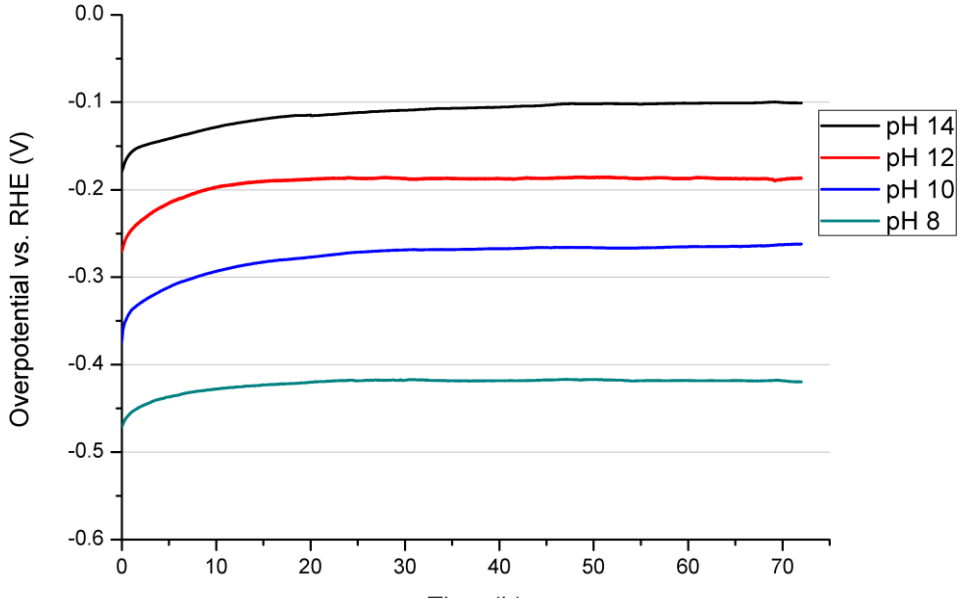

Appendix Fig. 3. Transient chrono-potentiometry for the lithium (Li) pH series. Activation times were visible for each in the series. pH 14.8 is not available due to solubility constraints

Appendix B – SEM images (roughening)

In this appendix several more examples of SEM images where surface roughening is clearly visible are presented. In total there have been taken more than a 100 SEM images (before and after catalysis). However, presenting them all would not of additional value so only a few series are shown here.

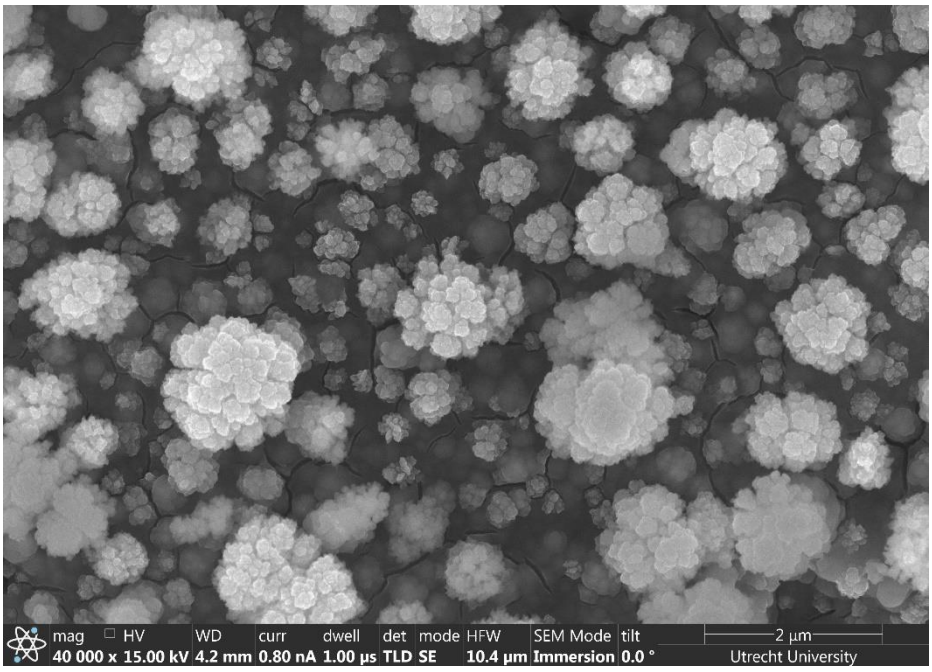

Appendix Fig. 4. SEM image before catalysis (JD01)

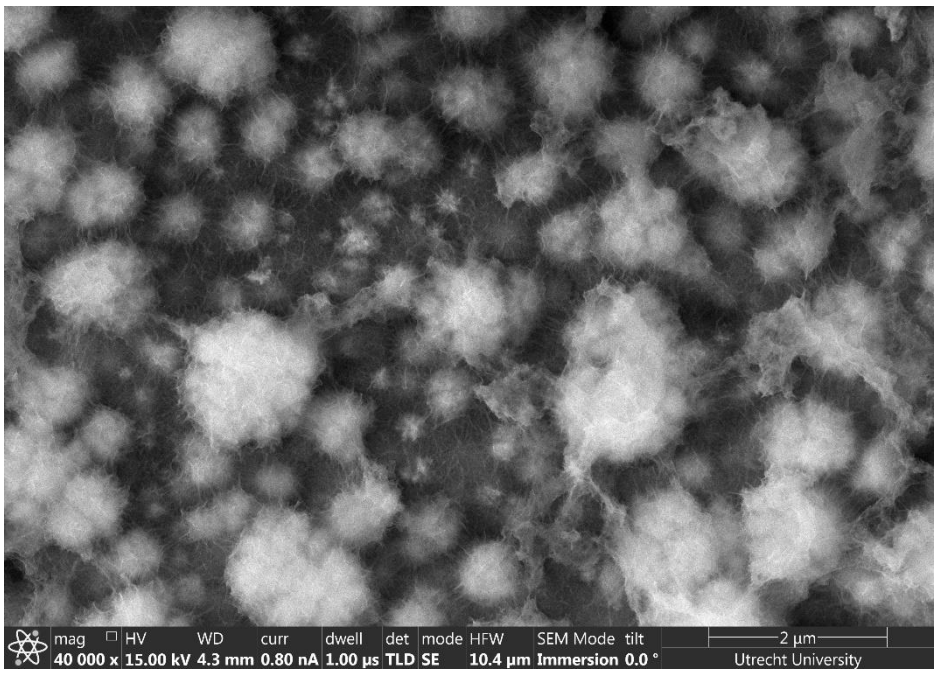

Appendix Fig. 5. SEM image after catalysis (JD01) in 1M NaOH after 72 h of catalysis

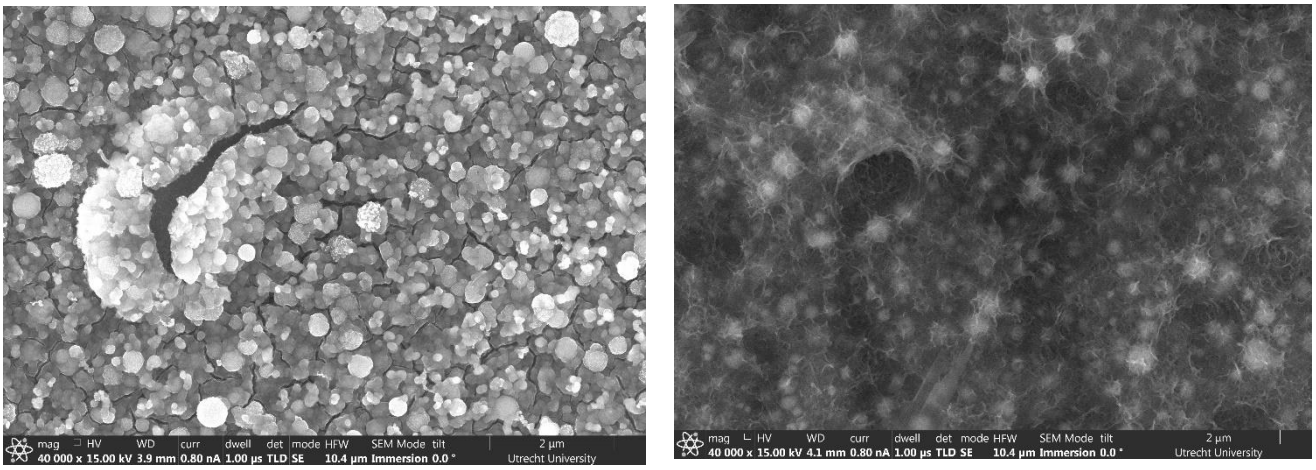

Appendix Fig. 6. SEM image before and after catalysis (JD19) in 6M KOH after 72 h of catalysis

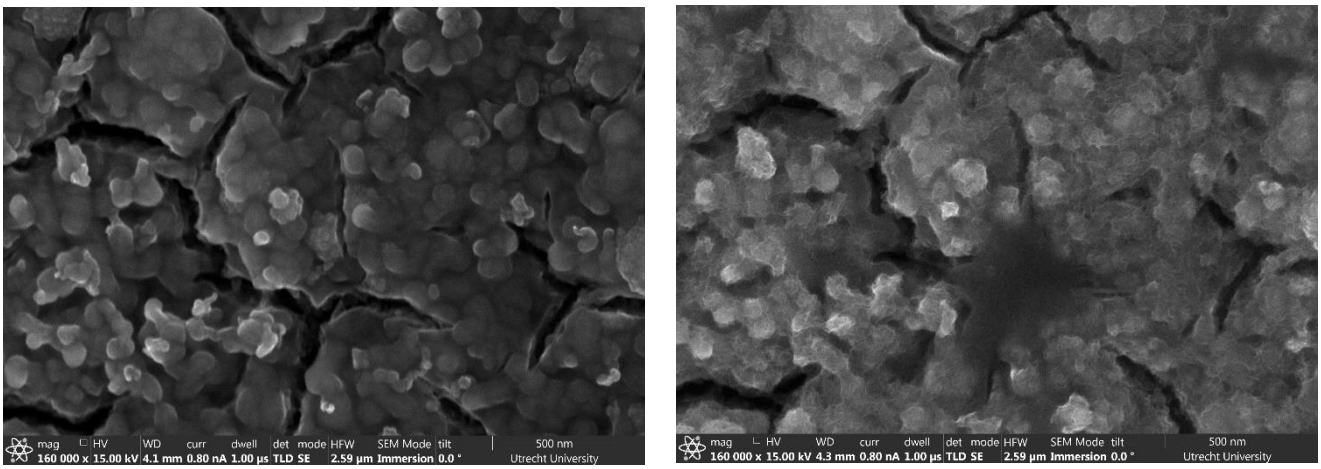

Appendix Fig. 7. SEM image before and after catalysis (JD24) in 6M LiOH after 72 h of catalysis

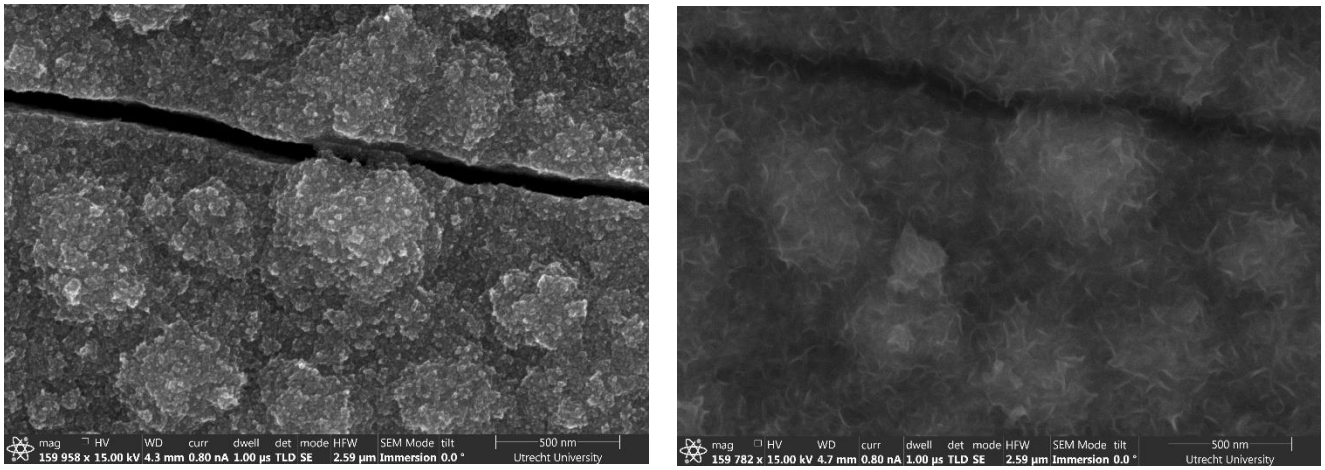

Appendix Fig. 8. SEM image before and after catalysis (JD11) in 1M KOH after 72 h of catalysis

Appendix C – ICP-AES

In this appendix the total list of ICP-AES results have been presented in a table. It should be noted here that the values in red are inaccurate due to the background being measured from 0.1 to 10 mg/L. The values in red have an error over 10% and should be taken as indicative.

Table 5. ICP-AES results for all the elements analysed for the tested samples after a catalysis time of 72 h.

	Cu 324.754	*K 766.491*	*Li 670.780*	*Mo 203.909*	*Na 589.592*	*Ni 231.604*	*Ti 334.187*
	mg/L	mg/L	mg/L	mg/L	mg/L	mg/L	mg/L
JD01	N/A	1.86	-0.00484	1.652	29305.5	0.712253	0.112965
JD02	N/A	16.868	-0.00275	1.742	30028.8	0.481398	0.170847
JD03	N/A	10.004	-0.00139	0.666939	28971.2	0.713952	0.047997
JD04	N/A	2.018	-0.00443	1.268	28369.5	1.142	0.130701
JD05	N/A	2.229	-0.00325	1.621	28284.6	0.009543	0.033019
JD06	N/A	7.975	0.007028	0.837907	27881.6	0.300447	0.075073
JD07	N/A	23.04	0.019696	2.422	47620.9	0.051384	0.08966
JD08	N/A	10.907	0.012828	1.074	46220.3	0.003226	0.175077
JD09	0.008401	7.666	0.012796	2.3258	1649.2	0.02285	0.22941
JD10	0.009365	14.433	0.018929	2.92522	1646.94	0.002295	0.176991
JD11	0.008405	8411.73	0.00468	3.684	47.869	0.005538	0.056095
JD12	0.006094	8051.04	0.009679	0.50625	37.908	0.017118	0.071029
JD13	0.003868	8564.73	-0.00296	2.342	13.833	0.025286	0.006013
JD14	0.003723	8078.01	-0.00159	0.583843	13.649	0.013445	0.007997
JD15	0.008097	8467.01	-0.00383	0.283324	11.833	0.761889	0.027931
JD16	0.011368	8664.96	-0.00379	1.902	12.355	0.946829	0.09894
JD17	0.009265	8853.05	-0.0034	2.066	10.72	1.109	0.062476
JD18	0.007952	9059.41	-0.00261	0.297413	8.73	0.335574	0.079311
JD19	0.03594	69891	-0.03521	13.7192	112.69	0	0.24563
JD20	0.0634	68939.5	-0.0366	12.5141	115.42	0	0.29494
JD21	0.008833	239.006	258.544	0.859205	40.19	-0.00186	0.083062
JD22	0.007694	216.639	250.942	0.244968	62.909	-0.00331	0.038834
JD23	0.004971	101.315	298.03	3.981	41.878	0.007315	0.012566
JD24	0.003982	61.122	300.048	3.535	42.227	-0.00415	0.006247
JD25	0.006744	2329.15	3.582	0.679579	76.438	-0.00761	0.157538
JD26	0.005507	162.153	303.937	0.170547	13.781	0.132249	0.10491
JD27	0.004333	122.213	307.414	0.895946	18.171	1.034	0.099213
JD28	0.003653	98.543	304.929	0.310913	22.266	0.234401	0.116136

Appendix D – *In-situ* UV-Vis cell

The aim of *in-situ* UV-Vis is to measure the leaching speed of molybdenum into the electrolyte solution. Molybdate is an absorbing species with a peak at 207 nm and a shoulder at 232 nm which is detectable using UV-Vis spectrometry. This makes quantification over time possible using a continuous measurement set-up. By combining a UV-Vis spectrometer and a potentiostat in a single set-up one can measure the leaching speed of molybdenum at different currents and potentials, which could possibly be linked to the increase in surface area and observed activation time. A special cell that is both compatible for electrolytic water-splitting and UV-vis spectrometry had to be designed and was hand-tailored by the Utrecht University glass-blower team (Appendix Fig. 9).
The design of the cell had to take several issues in account. First of all the molybdate absorb in the UV-region close to 200 nm. In this region, amorphous glass interacts with UV light, which required us to use quartz silica glass for the cell. We decided to use Suprasil quartz windows with a transmittance of >90% at a wavelength of 200 nm. The quartz windows have to be as flat as possible to reduce scattering in other directions. Secondly, the cell needed to have a known pathlength. This known pathlength is necessary according to Lambert-Beer's law.

$$Absorbance\ \left(log_{10}\frac{I_0}{I}\right) = \varepsilon \times l \times C$$

Where ε is the extinction coefficient, l the length of the cell in cm and C the concentration of the analyte. The l needs to be known to accurately determine the concentration molybdate that would leach from the electrode. The pathlength for our cell is 5 cm. Then, there needs to be room for three electrodes (working, counter and reference) to enable connection to a potentiostat. Finally, a gas inlet for argon flushing and gas outlet for pressure release had to be added for gas control.
All these different aspects were be put together in a single cell. The cell is presented in Appendix Fig. 9.

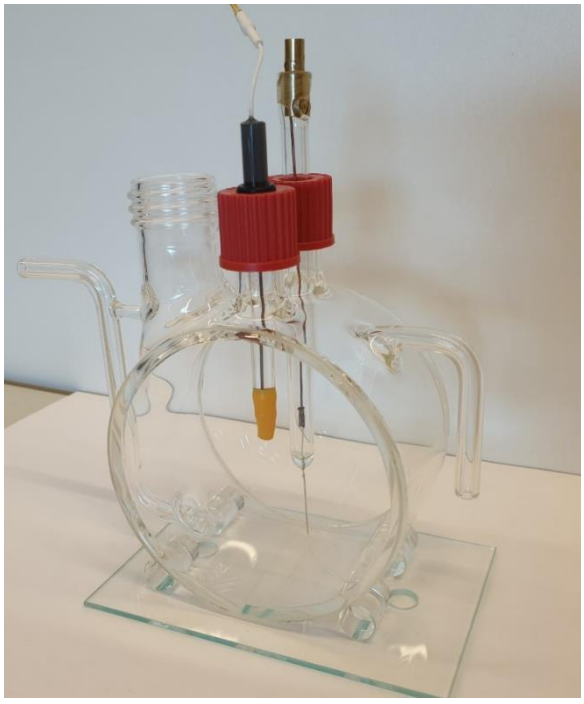

Appendix Fig. 9. The hand tailored in-situ UV-Vis cell

Appendix E – AFM images

1 M KOH – No current

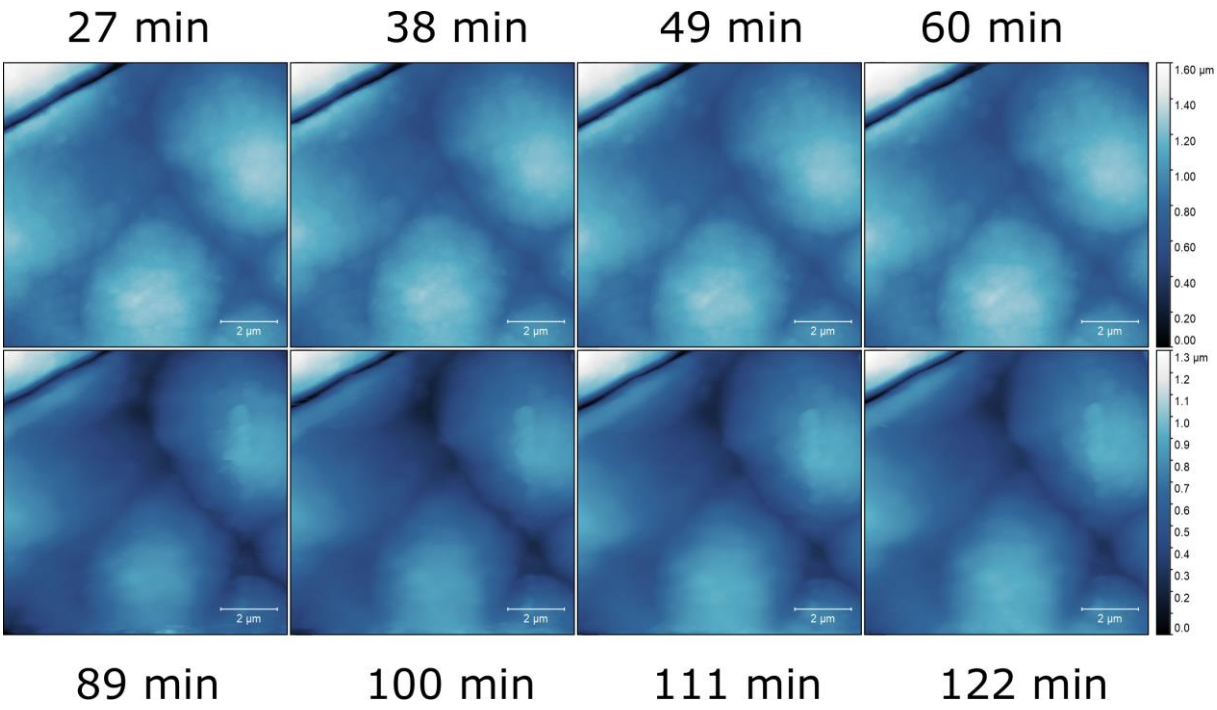

After 60 min tip was out of contact, re-established for 89 min but resolution seemed a bit lower
After 122 min, liquid evaporated, as could be seen by the droplet edge appearing on the optical microscope

0 M KOH - No current

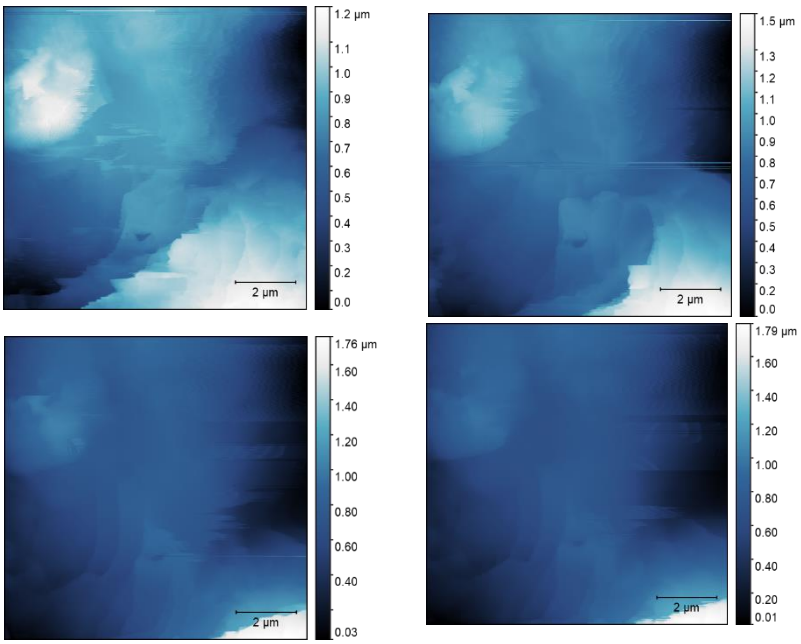

Slow start; first hour is missing
Not much Ni-Mo features found, could be pure substrate
Roughness seems to be fairly constant in last two pictures